OCS Study
BOEM 2014-1003

Intra-Americas Sea Nowcast/Forecast System Ocean Reanalysis to Support Improvement of Oil-Spill Risk Analysis in the Gulf of Mexico by Multi-Model Approach

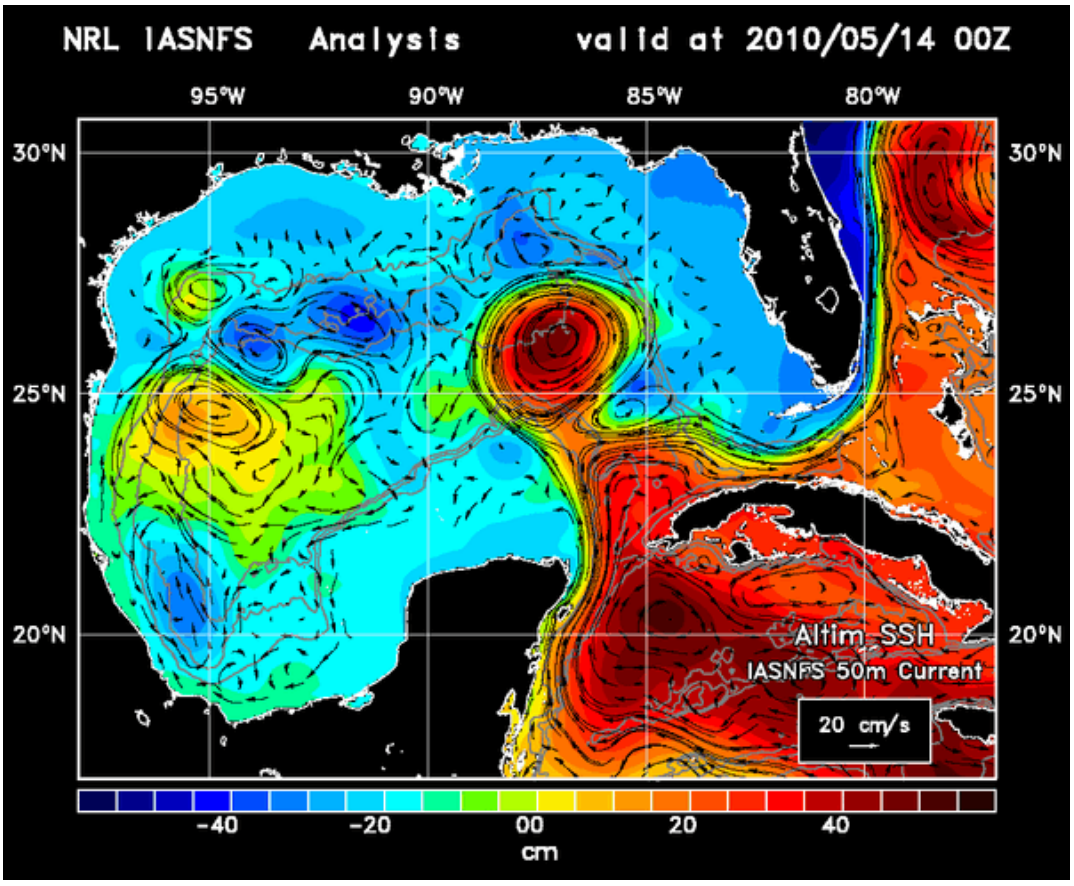

U.S. Department of the Interior

Bureau of Ocean Energy Management

Headquarters

Herndon, Virginia

Intra-Americas Sea Nowcast/Forecast System Ocean Reanalysis to Support Improvement of Oil-Spill Risk Analysis in the Gulf of Mexico by Multi-Model Approach

by
Dong S. Ko
Dong-Ping Wang

Prepared under BOEM Contract M12PG00030
by
Naval Research Laboratory, Oceanography Division
Stennis Space Center, Mississippi 39529
and
School of Marine and Atmospheric Sciences, Stony Brook University
Stony Brook, New York 11794

US Department of the Interior
Bureau of Ocean Energy Management
Headquarters

Disclaimer

This study was funded, in part, by the US Department of the Interior, Bureau of Ocean Energy Management, Environmental Studies Program, Washington, DC, through Inter-Agency Agreement Number M12PG00030 with the Naval Research Laboratory and the School of Marine and Atmospheric Sciences, Stony Brook University. This report has been technically reviewed by BOEM and it has been approved for publication. The views and conclusions contained in this document are those of the authors and should not be interpreted as representing the opinions or policies of the US Government, nor does mention of trade names or commercial products constitute endorsement or recommendation for use.

Report Availability

To download a PDF file of this Environmental Studies Program report, go to the US Department of the Interior, Bureau of Ocean Energy Management Environmental Studies Program Information System at http://www.boem.gov/Environmental-Stewardship/Environmental-Studies-Program-Information-System.aspx and search on OCS Study BOEM 2014-1003.

Citation

Ko, D. S. and Wang, D-P (2104) Intra-Americas Sea Nowcast/Forecast System Ocean Reanalysis to Support Improvement of Oil-Spill Risk Analysis in the Gulf of Mexico by Multi-Model Approach, Department of the Interior, Bureau of Ocean Energy Management, Herndon, VA. BOEM 2014-1003.

About the Cover

This shows the IASNFS reanalysis water currents below the surface boundary layer at 50 m depth (in black vectors) superimposed over color-coded satellite altimeter sea surface height (SSH) for May 14, 2010. This analysis indicates that the IASNFS current follows the altimeter SSH remarkably well, even when the Gulf Loop Current was evolving rapidly.

Acknowledgments

We greatly acknowledge the support of the Department of the Interior's Bureau of Ocean Energy Management under contract No. M12PG00030 for sponsoring this reanalysis effort. We thank Walter Johnson for the plots from current moorings, and our Contract Officer's Representative Zhen Li for her support and guidance. The development and operation of IASNFS were supported by the National Aeronautics and Space Administration (NASA), the National Oceanic and Atmospheric Administration (NOAA), the Environmental Protection Agency (EPA), Department of Energy, Gulf of Mexico Research Initiative and the U.S. Navy.

Contents

List of Figures

List of Tables

Abbreviations and Acronyms

AVISO	Archiving, Validation and Interpretation of Satellite Oceanographic (data)
BOEM	Bureau of Ocean Energy Management
DBDB2	Digital Bathymetry Data Base in 2-min
FNMOC	Fleet Numerical Meteorology and Oceanography Center
GMT	Generic Mapping Tools
GDEM	Generalized Digital Environmental Model
GOM	Gulf of Mexico
IASNFS	Intra-Americas Sea Nowcast/Forecast System
MCSST	Multi-Channel Sea Surface Temperature
MODAS	Modular Ocean Data Assimilation System
MOODS	Master Oceanographic Observation Data Set
NASA	National Aeronautics and Space Administration
NAVO	Navy Oceanography Office
NCOM	Navy Coastal Ocean Model
NDBC	National Data Buoy Center
NGDC	National Geophysical Data Center
NGOM	NOS Gulf of Mexico Model
NOAA	National Oceanic and Atmospheric Administration
NOGAPS	Navy Operational Global Atmospheric Prediction System
NOS	National Ocean Service
NRL	Naval Research Laboratory
OCS	Outer Continental Shelf
OSRA	Oil Spill Risk Analysis
POM	Princeton Ocean Model
SSH	Sea Surface Height
SSS	Sea Surface Salinity
SST	Sea Surface Temperature
UTC	Coordinated Universal Time

1 Introduction

The Bureau of Ocean Energy Management (BOEM) is responsible for analysis of potential oil-spill impact to the environment prior to sales of lease for oil and gas exploration in the Gulf of Mexico (GOM) Outer Continental Shelf (OCS). To estimate the probability of potential oil spill that has an impact on environmental resources in the GOM OCS, the high-resolution gridded products of surface currents and winds in the Gulf of Mexico are needed to drive an oil-spill trajectory model. Currently, the Bureau's Oil Spill Risk Analysis (OSRA) model relies on the surface currents generated from one single Gulf of Mexico circulation model. The deterministic approach with one set of surface current and wind input to the OSRA model could be improved by incorporating multiple sets of input from different proven ocean models, as the ocean model output is subject to uncertainties in surface winds from various atmospheric products. A multi-model approach has been proposed by conducting ensemble OSRA model runs that include different sets of surface currents simulated by well-validated Gulf of Mexico ocean circulation models and their corresponding wind forcing. An ensemble of model solutions will be statistically analyzed to understand the uncertainty in the probability of the potential impact of oil spill on the environment.

The outcome will improve the accuracy of the oil spill risk analysis for the projected areas of OCS operations and provide more accurate information for BOEM on the oil spill risk management and contingency planning in the Gulf of Mexico. The method developed could be employed in other OCS Regions as well.

To achieve this goal, several different sets of model-simulated surface currents and their corresponding surface winds in the Gulf are needed to drive the Oil Spill Risk Analysis model. A ten-year ocean re-analysis for the Gulf of Mexico which includes sea level variation, ocean current, sea temperature and salinity has been produced to support this effort (Ko and Li, 2013), applying the Naval Research Laboratory (NRL) Intra-Americas Sea Nowcast/Forecast System (IASNFS) (Ko et al., 2003; Ko, 2009). The reanalysis was derived with Navy Operational Global Atmospheric Prediction System (NOGAPS) (Rosmond, 1992) atmospheric forcing and assimilation of satellite altimeter sea surface height and multi-channel sea surface temperature (MCSST) measurements. The open boundary conditions were taken from Navy's Global Navy Ocean Coastal Model (NCOM) (Rhodes et al., 2002).

This report is organized as follows. General attributes of ocean model are presented in section 2. Details of ocean model setup are provided in section 3. The NOGAPS atmospheric forcing is described in section 4. The data and data assimilation are discussed in section 5. The output of reanalysis is outlined in section 6. The reanalysis is examined in

section 7 that includes evaluations against satellite altimeter measurement, coastal sea level from tide gauges, sea surface temperature from buoys and satellite, and ocean current from moorings. Summary is given in section 8.

2 Ocean Model

IASNFS used to conduct this reanalysis is an application of the US NRL's Ocean Nowcast/Forecast System (Ko et al., 2008). The system is an integration of a data-assimilating, dynamical ocean model, a statistical data-analysis model, and various data streams for ocean bathymetry, climatological data, surface forcing, open boundary forcing, and observations for data assimilation. The dynamic ocean model in the IASNFS is NCOM (Martin, 2000), developed at Naval Research Laboratory and in operation at the US Naval Oceanographic Office (NAVO) in various configurations (Rhodes et al., 2002).

NCOM is a hybrid sigma/z-level primitive equation, free-surface model applying the hydrostatic, incompressible, and Boussinesq approximations. This model is similar in its physics and numeric to the Princeton Ocean Model (POM) (Blumberg and Mellor, 1987), but uses an implicit treatment of the free surface. The model equations include a source term that is used for river inflows. There are options for higher-order treatment of some terms, e.g., third-order upwind for advection (Holland et al., 1998), which was used for this reanalysis. Vertical mixing is computed using the Mellor-Yamada Level 2 scheme (Mellor and Yamada, 1974), modified for use over the entire water column. The equation of state is that of Mellor (1991).

The Intra-Americas Sea Nowcast/Forecast System was developed at the Naval Research Laboratory and in continuous real-time operation from 2003 to 2012, providing 72-h forecast on a daily basis (Ko et al., 2003). During the 2010 Deep Water Horizon oil spill at Gulf of Mexico, IASNFS is one of the backbone models that provided real-time surface current forecast to National Oceanic and Atmospheric Administration (NOAA) for oil trajectory prediction. Figure 1, provided by NOAA Office of Coast Survey, shows the predicted particle distributions for May 20, 2010, initialized from May 17 satellite analysis (shown in gray) using surface currents from 4 available ocean models. The prediction applying IASNFS forecast (Figure 1b) performs very well compared to predictions using other models.

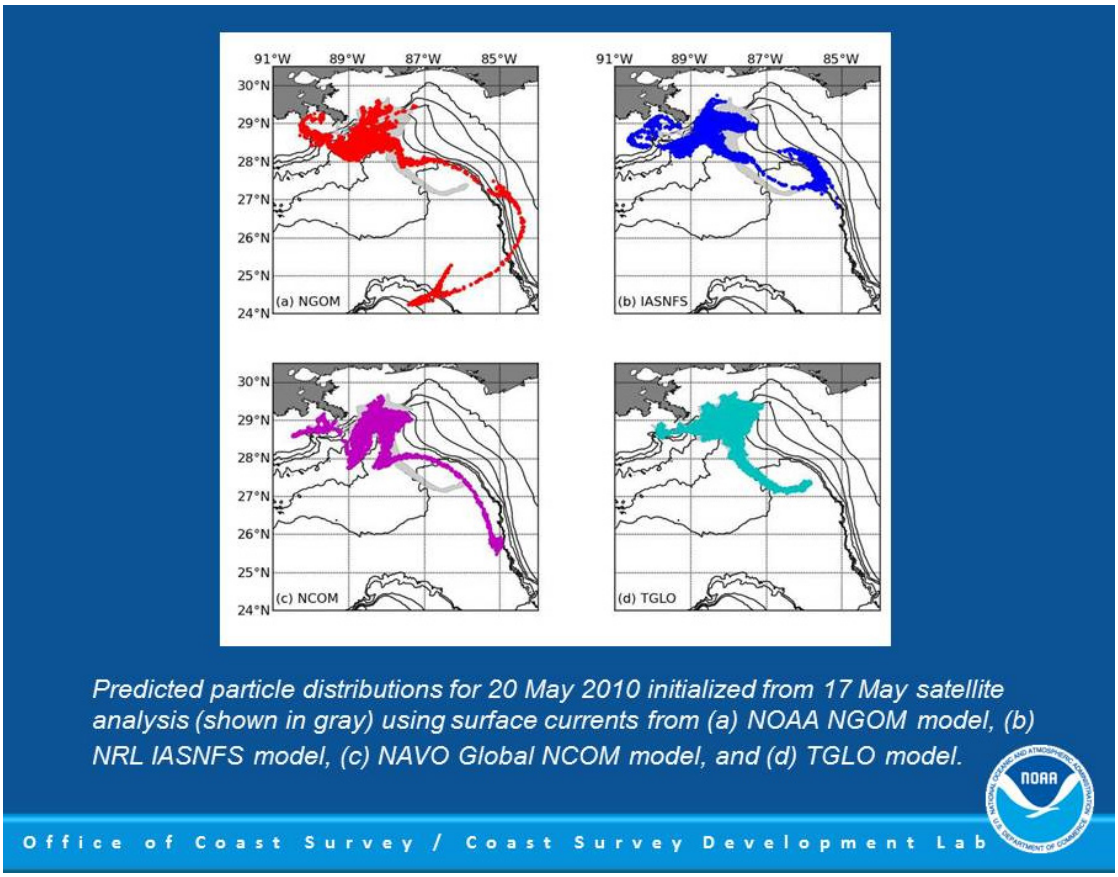

Figure 1. Predicted particle distributions for May 20, 2010 from NOAA during Deep Water Horizon oil spill at Gulf of Mexico using surface currents from (a) NOAA NGOM model, (b) NRL IASNFS model, (c) NAVO Global NCOM model, and (d) Texas General Land Office (TGLO) Model

In addition to real-time applications, IASNFS and its embedded high-resolution coastal grids have been applied for a wild variety of studies. For example, it was used to study colored dissolved organic matter dynamics in the northern Gulf of Mexico (Chaichitehrani et al., 2014), coastal and marine ecological classification for pelagic habitats in the Gulf of Mexico (Allee et al., 2014), nutrient transports and source/sink dynamics on the inner Louisiana continental shelf (Lehrter et al., 2013), effects of Hurricane Ike on the Louisiana-Texas coast (D'Sa et al., 2011), forecasting of coastal optical properties using satellite ocean color (Arnone et al., 2007; 2010), developmental strategy for effective sampling to detect possible nutrient fluxes in oligotrophic coastal reef waters in the Caribbean (Mendoza et al., 2009), short-term influences on suspended particulate matter distribution in the northern Gulf of Mexico (D'Sa and Ko, 2008), the statistical models for sediment/detritus and dissolved absorption coefficients in coastal waters of the northern Gulf of Mexico (Green et al., 2008), restoring of suspended particles in ocean using satellite optical images and forecasting particle fields (Haltrin et al., 2007), and assessment of data

assimilative ocean models in the Gulf of Mexico using ocean color (Chassignet et al., 2005).

3 Ocean Model Setup

The ocean model setup for the reanalysis production is identical to the setup for the real-time operation (Ko et al., 2003; Ko, 2009).

3.1 Ocean Model Domain and Model Grid

The IANSFS model domain covers entire Gulf of Mexico, Straits of Florida, the Caribbean Sea and part of western North Atlantic Ocean with domain from 5.8°N to 30.7°N and from 97.0°W to 55.0°W (Figure 2, grid in red). The IASNFS is embedded in the Navy's Global NCOM model (Figure 2, grid in blue) (Rhodes et al., 2002). The IASNFS model grid follows the longitude-latitude lines in Mercator projection with ~1/24° horizontal resolution. The model grid is kept in square (in unit of km), i.e., $\Delta x = \Delta y$ at center of each grid to better resolve eddy motions which generally do not have a preferred direction. The grid size varies with latitude, decreasing from south toward north. It ranges from ~6.5 km at the model's southern boundary to ~5.6 km at the model's northern boundary. The average horizontal resolution is about 6 km in the Gulf of Mexico.

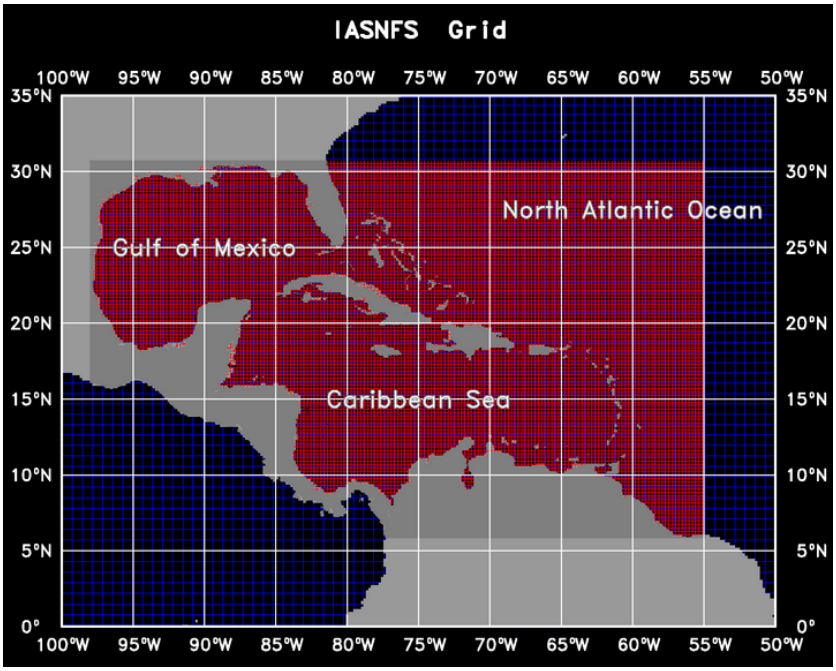

Figure 2. IASNFS model domain and grid. The IASNFS grid (in red) is embedded in the Global NCOM (in blue). The horizontal resolution is ~1/24 ° increasing from south to north depending on the latitude. It is about 6 km in the GOM. For both GNCOM and IASNFS, every fourth grid is plotted.

Vertically, there are 41 sigma-z levels (Table 1) in the model, with thinner layers in the upper water column to better resolve upper ocean variations. Nineteen sigma layers are used from the surface down to a depth of 137.87 m, and z-levels are used below. This vertical grid is like a regular sigma coordinate grid on the continental shelf, in the water shallower than 137.87 m, and is similar to a level grid in deeper ocean. The vertical grid is uniformly stretched from the surface downward with a maximum thickness of the surface layer of 1 m. The vertical levels and layer thickness are listed in Table 1. The advantage of using sigma-z level hybrid vertical coordinates is that it follows the terrain over the continental shelf for better resolving topographic effects, and it becomes the level grid in deep water, avoiding the pressure gradient error in a pure sigma coordinate model (Haney, 1991). The disadvantage is that it may not adequately resolve the bottom boundary layer on the continental slope below the shelf break where z-level is applied.

Table 1. Vertical levels and layer thickness used in IASNFS. The top 20 levels are sigma level, σ, that follow the terrain on the shelf: $\sigma = z / h^*$, where z is the depth of levels and h* is minimum of water depth, or 137.87 m.

Level #	Level (m)	Layer Thickness (m)
1	0.00	1.00
2	1.00	1.19
3	2.19	1.42
4	3.61	1.68
5	5.29	2.00
6	7.29	2.38
7	9.68	2.83
8	12.52	3.38
9	15.89	4.02
10	19.91	4.78
11	24.69	5.69
12	30.37	6.77
13	37.14	8.05
14	45.18	9.58
15	54.76	11.39
16	66.16	13.56
17	79.71	16.13
18	95.84	19.19
19	115.03	22.84
20	137.87	27.17
21	165.04	32.33
22	197.36	38.46

Level #	Level (m)	Layer Thickness (m)
23	235.83	45.76
24	281.59	54.45
25	336.03	64.78
26	400.82	77.08
27	477.90	91.71
28	569.60	109.12
29	678.72	129.83
30	808.55	154.47
31	963.02	183.79
32	1146.81	218.68
33	1365.48	260.18
34	1625.66	309.57
35	1935.23	368.33
36	2303.55	438.24
37	2741.79	521.42
38	3263.21	620.39
39	3883.59	738.14
40	4621.74	878.26
41	5500.00	

3.2 Model Topography

The IASNFS model ocean topography (Figure 3) is derived from the NRL global Digital Bathymetry Data Base 2-min (DBDB2) (http://www7320.nrlssc.navy.mil/DBDB2_WWW/). The topography was interpolated onto the model grid, applying Akima cubic splint to prevent overshoots or "wiggles" (Akima, 1970). The land-sea grid separation was determined based on the finest Generic Mapping Tools (GMT) vector coastline data (http://www.soest.hawaii.edu/gmt/). Some modifications were made to open up the narrow waterways such as the Rigolets in Louisiana that connects Lake Pontchartrain to Lake Borgne and then to the Gulf of Mexico. The model ocean topography was further improved by assimilating NOAA National Geophysical Data Center (NGDC) bathymetry data from hydrographic surveys (http://www.ngdc.noaa.gov/mgg/bathymetry/). The model topography is truncated to the levels (Table 1) off shelf break (>137.87 m) to a maximum depth of 5500 m and the minimum water depth is set to 5 m.

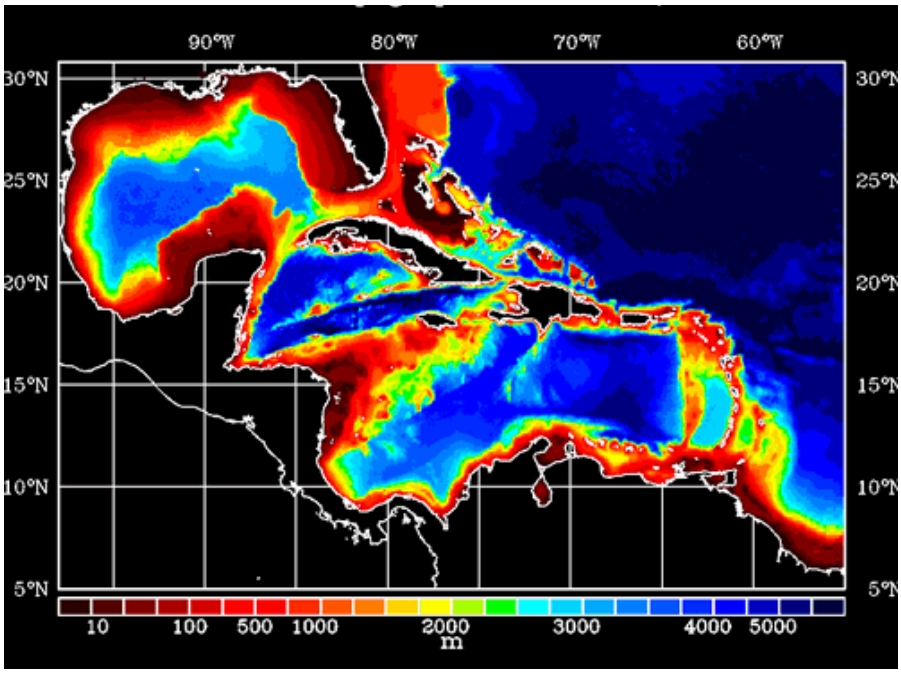

Figure 3. IASNFS model topography.

3.3 Initial and Boundary Conditions

Initial conditions for sea surface height (SSH), current velocity (u and v), temperature (T), and salinity (S) for October 1, 2001 were taken from the IASNFS restart file that was archived from model start-up for the real-time run. The reanalysis was conducted for the period from October 1, 2001 to January 1, 2013; the first 3 months of output was discarded.

The boundary conditions (BCs) at the open boundary along the northern and eastern model boundaries were obtained from Global NCOM 6-hourly hindcast archive. The Global NCOM was developed at NRL and in operation at NAVO from 2000 to 2013 (Barron et al., 2004). Global NCOM provides IASNFS with SSH, u, v, T and S for BCs. The numerical treatment of the BCs includes forced radiation BC for the SSH, η, and depth-averaged normal velocity, u, modified from Flather and Proctor (1983),

$$u = u_G \pm c\,(\eta_G - \eta)/h,$$

where subscript G denotes variables from Global NCOM, and c is the barotropic wave phase speed: $c = \sqrt{gh}$, with g being the gravitational constant and h the water depth. On the western/southern boundary the positive sign is applied; on the eastern/northern boundary the negative sign is applied (applicable to IASNFS).

For the BCs of tangential velocity, v, and T and S, the first-order-upwind advection scheme was utilized. A relaxation to the T and S fields of the global model was applied along the

open boundary over 48 model grids or about twice the baroclinic deformation radius with a linear weighting, which increases from interior toward the boundary. The normal baroclinic velocity at the open boundary was computed using the model's full velocity equation, except that advection for normal velocity was only computed normal to the boundary with first-order-upwind scheme.

3.4 River and River Runoff

Within IASNFS domain there are several rivers with very large discharges. On average, the Mississippi River and Atchafalaya River at the Gulf Coast discharge 14,720 m^3/s and 6,310 m^3/s of water into Gulf of Mexico, respectively. The Orinoco River in Venezuela has an even larger discharge at about 33,000 m^3/s which is ranked fourth in the world. The river discharge has a profound influence on the sea water salinity as well as on the circulation, particularly in the coastal region (e.g., Hetland, 2010 and references therewithin). There are 140 rivers and streams in the IASNFS that discharge into model domain. Rivers are input into the ocean model as a volume source with specified salinity and temperature and vertical flow distribution. The salinity of river water for all rivers was set to 0 except that it was set to S = 10 for the Intracoastal Waterway at Industry Canal, New Orleans, Louisiana to simulate the salt water intrusion in Lake Pontchartrain.

Real-time river water temperature is in general unavailable in the IASNFS domain except for the Mississippi River. The water temperature for other rivers on the Gulf Coast was prescribed according to the measured temperature of Mississippi River and the monthly temperature climatology, weighted by the distance to the Mississippi River mouth. Monthly climatology was applied to the rest of rivers. All river temperatures were adjusted with satellite MCSST.

Real-time river flow data are commonly available for the rivers at the Gulf coast and Florida coast. The daily average river flow data from Army Corps of Engineers (http://www.mvn.usace.army.mil/eng/edhd/wcontrol/wcmain.asp) for the Mississippi River at Tarbert Landing, Mississippi, and for the Atchafalaya River at Simmesport, Louisiana, were used (Figure 4). The Mississippi River runoff was discharged into model domain spreading by the following percentages: Southwest Pass (29.7%), South Pass (12.9%), Pass A Loutre (11.7%), Cubits Gap (11.1%), Baptiste Collette Bayou (9.8%), Grand and Tiger Pass (9.4%), West Bank (4.5%) and West Bay Diversion (4.1%). The balance of the Mississippi River runoff was distributed among nearby smaller streams and outlets. The Atchafalaya runoff was discharged into model domain at Low Atchafalaya and Wax Lake outlets and the nearby smaller streams and outlets. Real-time river flow data are also available for rivers located along coast from Texas to Florida from the US Geological Survey (USGS) (http://waterdata.usgs.gov/nwis). Daily average river flow data for

Colorado River (TX), Trinity River (TX), Neches River (TX), Sabine River (TX/LA), Calcasieu River (LA), Mermentau River (LA), Vermilion River (LA), Tangipahoa River (LA), Bayou Lafourche (LA), Pearl River (LA/MS), Biloxi River (MS), Mobile River (AL), Escambia River (FL), Apalachicola River (FL), Suwannee River (FL) and Saint Johns River (FL) were used. For the rest of the rivers in IASNFS domain that do not have real-time measurement for the re-analysis period, the monthly climatology compiled from World Meteorology Organization (WMO) Global Runoff Data Center (http://blogs.esri.com/esri/arcgis/2012/01/17/wmo-global-runoff-data-centre/) river discharge data archive was applied.

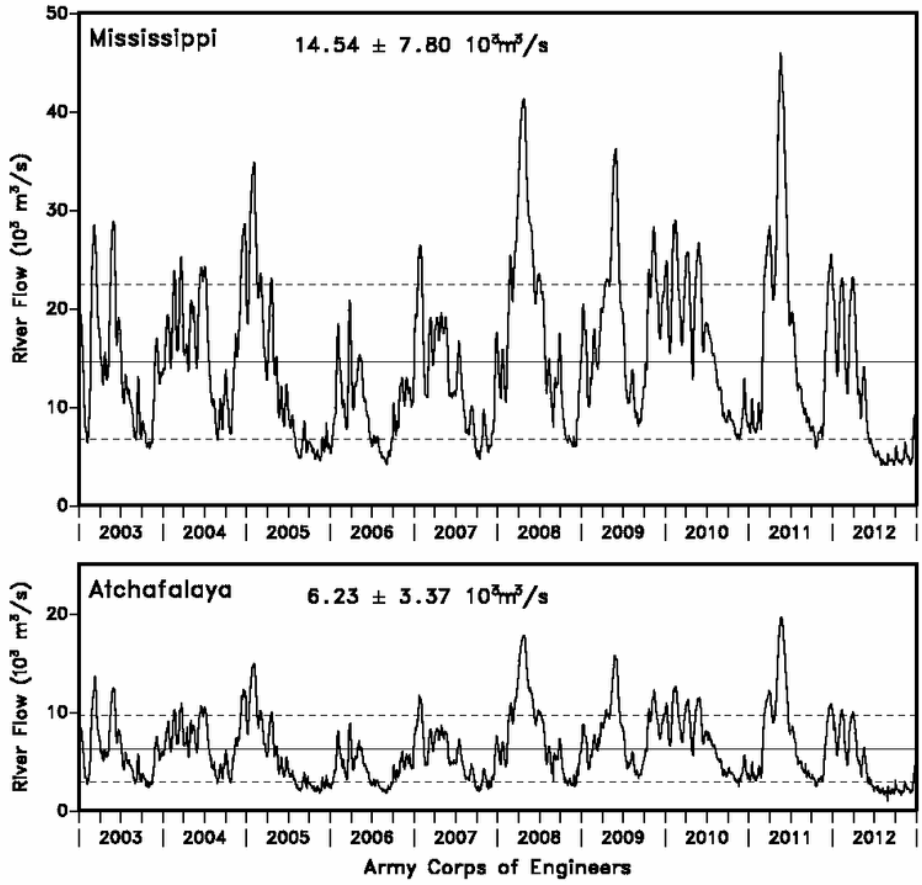

Figure 4. Real-time daily average river flow data from Army Corps of Engineers for Mississippi River at Tarbert Landing, Mississippi, and for Atchafalaya River at Simmesport, Louisiana.

The river discharge, in addition to seasonal and interannual variations, often fluctuates strongly over short period of time (e.g., Figure 4) corresponding to major flood events. It is advantageous to use real-time river flow data for realistic simulation.

3.5 Tidal Forcing

In NCOM, the tidal forcing based on tidal potential and tidal harmonics is available. Eight tidal harmonics (K_1, O_1, P_1, Q_1, M_2, S_2, K_2, and N_2) are used. These were taken from Oregon State University tidal database that were derived from satellite altimetry data (Egbert and Erofeeva, 2003). Tides are applied to model depth-averaged normal velocity, *u*, at open boundary by combining forcing from global model (Section 3.3):

$$u = (u_G + u_t) \pm c\,[(\eta_G + \eta_t) - \eta]/h,$$

where subscript *t* denotes variables from tidal model. Tidal potentials are applied to entire model grid. For this reanalysis run, tidal forcing was not applied.

4 Atmospheric Forcing

The atmospheric forcing applied for this re-analysis was the real-time NOGAPS product. It consists of fields of sea level air pressure, surface wind stress, solar radiation and surface total heat flux (Figure 5). The surface total heat flux includes latent heat flux, sensible heat flux and solar radiation. NOGAPS is the Navy's operational global weather forecast model operated by the Fleet Numerical Meteorology and Oceanography Center (FNMOC) which twice a day produces 120 h forecasts at 00 and 12 UTC. The NOGAPS horizontal resolution was about 1° and, since September 2004, has improved to 0.5° resolution. The 3-hourly products, combination of analyses at 00 and 12 UTC and 3-h, 6-h and 9-h forecasts, were used. The highest temporal data available is used to better simulate short-time synoptic scale variations.

The NOGAPS sea level air pressure, wind stress, solar radiation and heat flux were interpolated from the global grid onto the IASNFS grid applying Akima cubic splint, and converted to model units. There are often large differences in the surface wind stress and heat flux between land and sea (Figure 5b and 5d). Those land values were removed and filled with nearby ocean values before interpolation to prevent contamination by the land-based data (Ko et al., 2008).

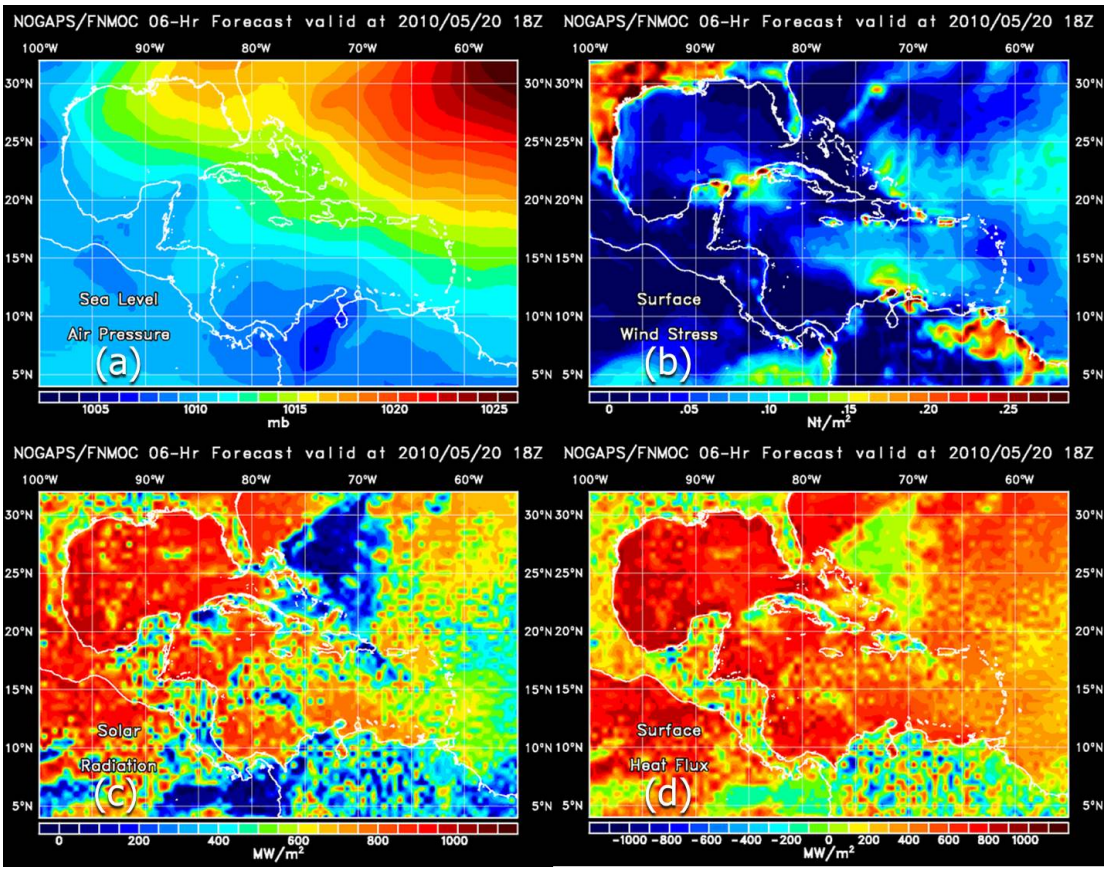

Figure 5. Atmospheric forcing fields of 6-h forecast from 12 UTC valid at 18 UTC May 20, 2010 from NOGAPS: (a) sea level air pressure, (b) surface wind stress, (c) solar radiation and (d) surface total heat flux.

Solar radiation was applied separately from the surface heat flux since solar radiation penetrates below the ocean surface and may have impact on the vertical mixing and sea surface temperature. Jerlov (1964) oligotrophic oceanic water type IA, which is commonly used for the open ocean, was applied for solar penetration. Applying a uniform water type is sufficient for most oceans, particularly in deep water. Occasionally, there may be overheating near the bottom in extreme shallow water, owing to excessive solar penetration. To account for spatial variability in water column absorption, e.g., higher absorption in river plume and inshore regions related to higher concentrations of chlorophyll a, chromophoric dissolved organic matter, and suspended particulate matter, Lehrter et al. (2013) used light attenuation estimated from Moderate Resolution Imaging Spectroradiometer onboard the Aqua satellites to correct the near-bottom overheating in coastal waters over Louisiana shelf. The satellite data, however, is not available for the entire period of the reanalysis, and no correction is made for the extreme shallow water.

An adjustment of the rest of the surface heat flux (solar radiation excluded) was applied proportional to the difference between the MCSST analysis (Section 5.1.2) and the model sea surface temperature (SST) divided by surface layer thickness, at a rate of 4 m/d. In addition, a weaker correction was applied based on the difference between the monthly climatological SST and the model SST (Ko et al., 2008).

The surface salinity flux was computed based on the difference between the Modular Ocean Data Assimilation System (MODAS) surface salinity analysis (Section 5.1) and the model sea surface salinity (SSS) divided by surface layer thickness, at a rate of 0.333 m/d and on the difference between the monthly climatological SSS and the model SSS.

Relaxation time of 30 days was used for the adjustments with climatology. The adjustment with climatological SST and SSS is to prevent bias that may exist in the NOGAPS heat fluxes, MCSST and MODAS SSS analysis. The monthly temperature/salinity climatology data was taken from Navy's global climatological data system, Generalized Digital Environmental Model (GDEM) (Carnes, 2009), and interpolated onto the model grid for the application.

5 Data Assimilation

Satellite altimeter SSH and MCSST observations were applied for the data assimilation. The MODAS was employed to produce the three-dimensional ocean temperature and salinity analyses from satellite altimeter SSH and MCSST. IASNFS then assimilated the analyses by continuous modification of model temperature and salinity toward the analyses, combined with scale separation.

5.1 Data and Data Analysis

5.1.1 Satellite Altimeter Data

All available satellite altimeter along-track SSH measurements from TOPEX/Poseidon, ERS-1, ERS-2, Geosat Follow-On (GFO), Jason-1, Envisat, Jason-2 and Cyrosat-2 are retrieved and processed at NAVO in real-time. Each day, 30 days of processed along-track SSH data are gridded onto a 1/4° global grid between 80°S and 80°N applying an Optimal Interpolation (OI) scheme that accounts for the temporal and spatial correlations evaluated from along-track data (Jacobs et al., 2002). In the along-track SSH, the barotropic tides are not completely removed even after applying a tidal model. The tidal residuals, as well as the barotropic waves excited by wind pulses, are largely removed in the gridding process. We used altimeter SSH to estimate the subsurface temperature for data assimilation (Section

5.1.3). It is important to remove barotropic waves from SSH analysis since barotropic waves are not related to the subsurface temperature (Chapman et al., 2004). The dominant signals in the altimeter analysis are related to the oceanic mesoscale variations. The gridded altimeter SSH anomaly in the IASNFS domain for May 20, 2010 is displayed in Figure 6. It clearly shows SSH anomalies that are produced mainly by mesoscale eddies.

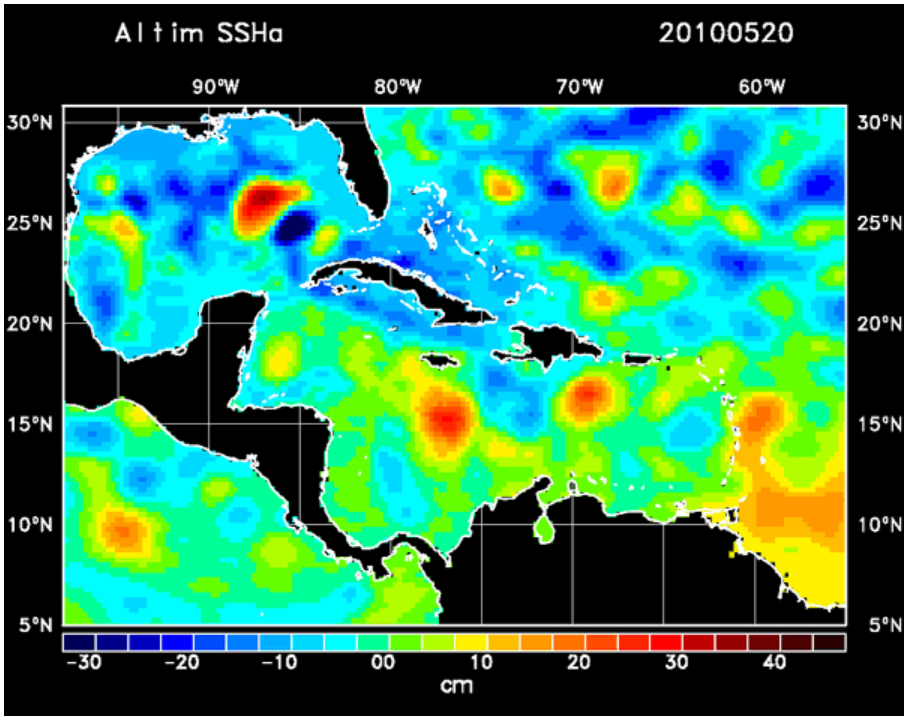

Figure 6. Satellite altimeter SSH anomaly analysis on 1/4° grid for May 20, 2010.

The gridded altimeter SSH, though at 1/4°, has a much coarser true spatial resolution. The satellite measurements are on fixed tracks repeated every 10 d, 17 d or 30 d. Although the spatial resolution of along-track measurement is less than 1 km, it is often averaged over ~100 km to reduce error; the off-track resolution is in order of 100 km depending on the satellite obit. The gridding can take advantage of simultaneous measurements of multiple satellites (e.g., Ducet et al., 2000). The spatial resolution for the merged gridded SSH from Archiving, Validation, and Interpretation of Satellite Oceanographic (AVISO) data, a similar product to the Navy's analysis, was estimated by Ducet et al. (2000) to be 150-200 km based on comparison of the wavenumber spectra in the Gulf Stream region. The spatial resolution should be similar for the NAVO product.

Temporal resolution of altimeter measurement is inversely correlated with its spatial resolution. While the temporal resolution increases, the spatial resolution decreases and vice versa. Overall, the gridded SSH that merges several altimeter measurements is adequate to resolve the mesoscale features in the Gulf of Mexico and Caribbean Sea where eddies and currents tend to be of larger scales.

5.1.2 Satellite MCSST Data

MCSST are derived from measurements of the Advanced Very High Resolution Radiometers (AVHRRs) onboard several NOAA satellites and the National Aeronautics and Space Administration (NASA) Polar Operational Environmental Satellite (POES) based on a regression model. The process for the MCSST are similar to that for the altimeter data except it is gridded on 1/8° global grid and with a data window of 5 days to compensate for missing data mainly from cloud blockage.

The MCSST analysis for May 20, 2010 is shown in Figure 7. It displays fine-scale features along the boundaries of Loop Current and Loop Current Eddy in the Gulf of Mexico and along the boundary of Florida Current in the Straits of Florida. Upwelling located off northern coasts of Yucatan Peninsula and South America can be clearly identified. However, in the summer seasons, those features generally cannot be observed from satellite data, owing to the obstruction by a thin surface skin layer of relatively uniform warm temperature.

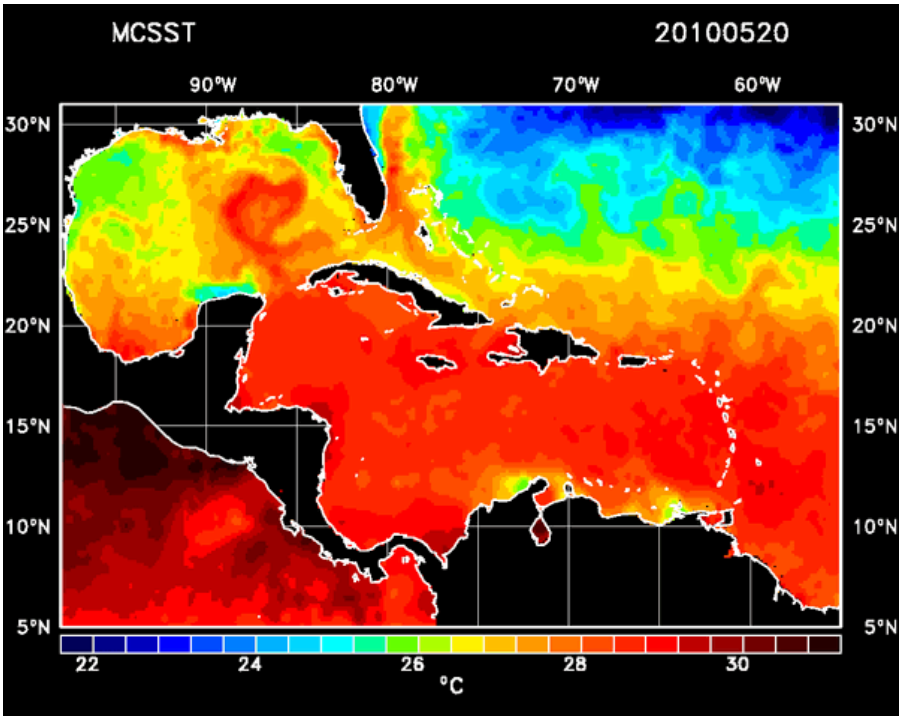

Figure 7. MCSST analysis on 1/8° resolution for May 20, 2010.

For the real-time operation, only the past 30 days of altimeter data and 5 days of MCSST data are used for analysis. For the reanalysis, ±30 days and ±5 days of data centered at the analysis time have been utilized to improve the analyses.

5.1.3 Data Analysis

The altimeter SSH and MCSST analyses were then used to produce 3D temperature and salinity analyses for data assimilation applying MODAS (Carnes et al., 1996; Fox et al., 2002). MODAS is a statistical model based on the regression between SSH/SST and subsurface temperature, and regression between temperature and salinity. The regressions were evaluated in a global scale employing a vast amount of temperature and salinity profile data in the NAVO Master Oceanographic Observation Data Set (MOODS) (Teague et al., 1987). The regressions are on the grids with variable resolution depending on location and data availability, and at the NAVO's standard depths for oceanography data used in MOODS.

The temperature profiles were estimated from SSH and SST analyses via regressions and the salinity profiles were then determined from temperature estimation via T-S correlation. The temperature and salinity profiles estimated at irregular grid of regression were mapped onto regular grid applying OI at each depth to construct 3D temperature and salinity analyses. The analyses were interpolated onto the model grid for data assimilation. Since the SSH and SST analyses were performed in daily basis, the 3D temperature/salinity analyses were produced each day and were interpolated in time in data assimilation when model was integrated forward in time.

5.2. Data Assimilation Scheme

The MODAS 3D temperature/salinity analyses were assimilated into the model using a vertical weighting function that reflects the oceanic temporal and spatial correlation scales and the relative confidence between the model forecasts and the analyses. In addition, scale separation is applied in data assimilation to preserve the fast-varying components.

The basic formula for data assimilation in IASNFS is,

$$T_{update} = T_{model} + \alpha\,(T_{analysis} - T_{model}),$$

where T is the temperature and α is a weighting function. The discrepancy between temperature analysis, $T_{analysis}$, and model prediction, T_{model}, is reduced by a friction defined by α to update the model temperature, T_{update}. This simple equation is the basis for a large group of data assimilation schemes. The major difference among schemes is in the determination of weighting function.

In the IASNFS, the weighting function is defined by

$$\alpha = \Delta t / t_{scale} \cdot f(z),$$

where Δt is the time interval for data assimilation and t_{scale} is the relaxation time scale. The value of α is between 0 and 1. If $\alpha = 0$, then there is no correction for the model prediction or no data assimilation. If $\alpha = 1$, then the model prediction is replaced with analysis.

A vertical function, $f(z)$, was applied to modify the weighting with respect to the depth. As shown in Figure 8, $f(z = 0) = 0$ at sea surface; it increases with depth to ~1 around 200 m. The function then decreases gradually from 700 m toward the deep ocean. Near the sea surface, the temperature and salinity variations are dominated by high temporal surface forcing and the mixing process. The surface mixing has very short temporal/spatial scales. Temperature/salinity analyses based on the satellite SSH/SST are essentially unable to resolve those scales, and therefore the weighting function at the surface is put to 0 and it is very small in the surface mixed layer. The signal in the satellite SSH analysis is predominated by the mesoscale variations in the upper ocean thermocline. The vertical weighting increases to ~1 around 200-700 m since mesoscale eddies or currents are most pronounced around those depths. The temperature or salinity variation in the deep ocean is very slow relative to the time scale for data assimilation; therefore the vertical weighting was reduced in deep depths.

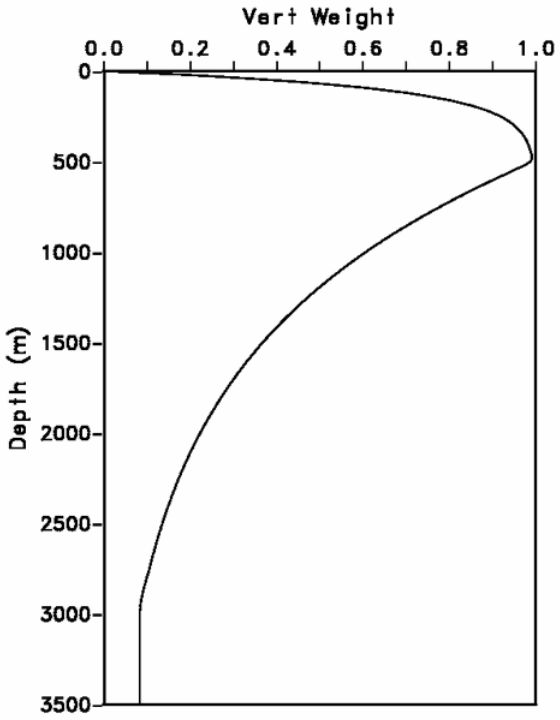

Figure 8. Vertical weighting function.

The temporal and spatial resolutions of 3D temperature and salinity analyses are inherited from the resolutions of the satellite SSH/SST analyses used. As discussed in previous session (Section 5.1) the SST analysis based on MCSST has a fairly good resolution during cooler season but the resolution of 3D T/S analyses are mainly dictated by the SSH analysis from altimeter data that have higher correlation with subsurface temperatures. The T/S analyses have a mesoscale resolution at best. To assimilate the coarse resolution of T/S analyses into a high-resolution model without utilizing a scale separation scheme (discussed below), will inadvertently remove higher frequency and shorter wavelength components of model's fields and will reduce its overall variability (Chapman et al., 2004). This effect can be clearly identified from the equation applied to the data assimilation by separating the low frequencies (*L*) from the high frequencies (*H*) in the model variables,

$$T_{update}(L) + T_{update}(H) = (T_{model}(L) + T_{model}(H)) + \alpha\,[T_{analysis}(L) - (T_{model}(L) + T_{model}(H))],$$

where analysis has only the low-frequency component, time scales of 10 days and longer, dictated by the altimeter repeat cycle, as discussed in previous section.

For low frequencies:

$$T_{update}(L) = T_{model}(L) + \alpha\,(T_{analysis}(L) - T_{model}(L)),$$

and for high frequencies:

$$T_{update}(H) = T_{model}(H) - \alpha\,T_{model}(H) = (1-\alpha)\,T_{model}(H).$$

It is obvious, no matter how small the value of α is or how it is determined, the high-frequency variations will be reduced over time unless $\alpha = 0$ or has no data assimilation. The remedy to avoid attenuation on the high-frequency variations is straightforward; which is to perform data assimilation with variables in similar scale separately or in scale separation. In our case, only data assimilation for the low frequencies was needed, since the temperature/salinity analyses used for data assimilation are of low frequencies (section 5.1),

$$T_{update} = (1-\alpha)\,T_{model}(L) + \alpha\,T_{analysis}(L) + T_{model}(H).$$

A running average applying a Gaussian time window of 5 d was applied to extract low-frequency component from model variables for data assimilation. The scale separation was also applied to the spatial domain using the Shapiro filter (Shapiro 1970, 1975). The separation in spatial scales however, is less effective because the spatial smoothing cannot be applied near the land and near topographic boundaries. For reanalysis, the Δt was set to

1 h, and t_{scale} to 5 d for data assimilation. The identical scheme is applied to temperature and salinity.

This data assimilation scheme is simple and very efficient. It consumes less than 5% of total model running time. Additional 5% of time is required to process the data for assimilation. The efficiency of the scheme is mainly due to the application of a constant weighting function that is not required to be reevaluated repeatedly.

The effectiveness of data assimilation is highlighted in Figures 9 and 10. In Figure 9, for 00 Universal Coordinated Time (UTC) May 14, 2010, the predicted current below the surface boundary layer at 50 m followed the altimeter SSH remarkably well although the altimeter data were not assimilated directly. Essence of mesoscale eddies and currents were well captured by the model, even during a time when the Loop Current was evolving rapidly. On the surface (Figure 10), the currents retained wind effects while under the influence of mesoscale eddies and currents. This shows the model is well-behaved under the data assimilation and is well constrained by the data.

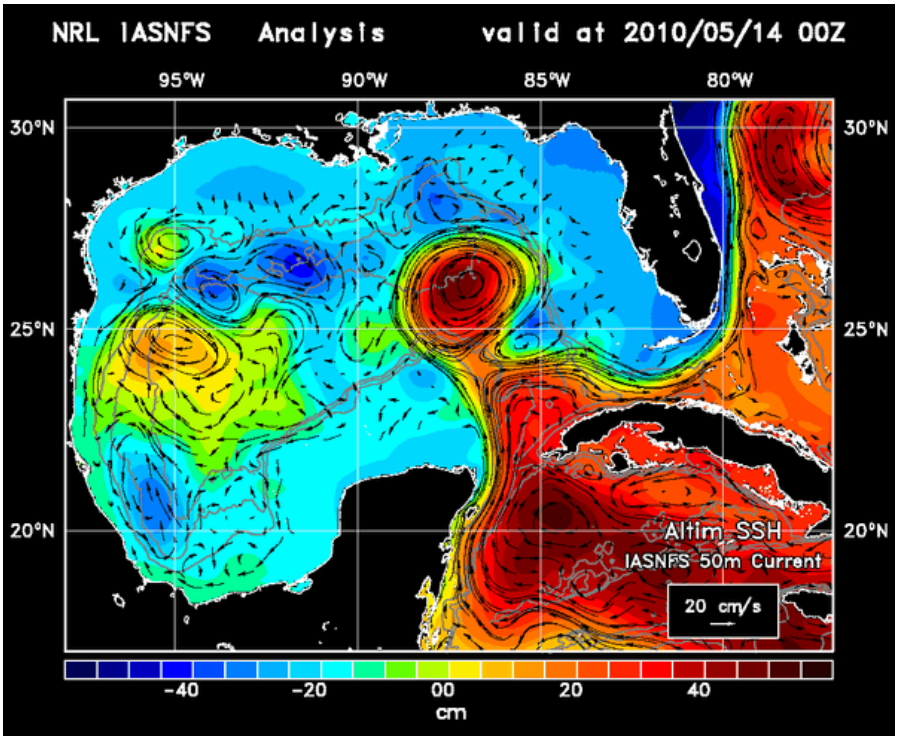

Figure 9. IASNFS reanalysis current at 50 m (black vectors) superimposed over satellite altimeter SSH (in colors).

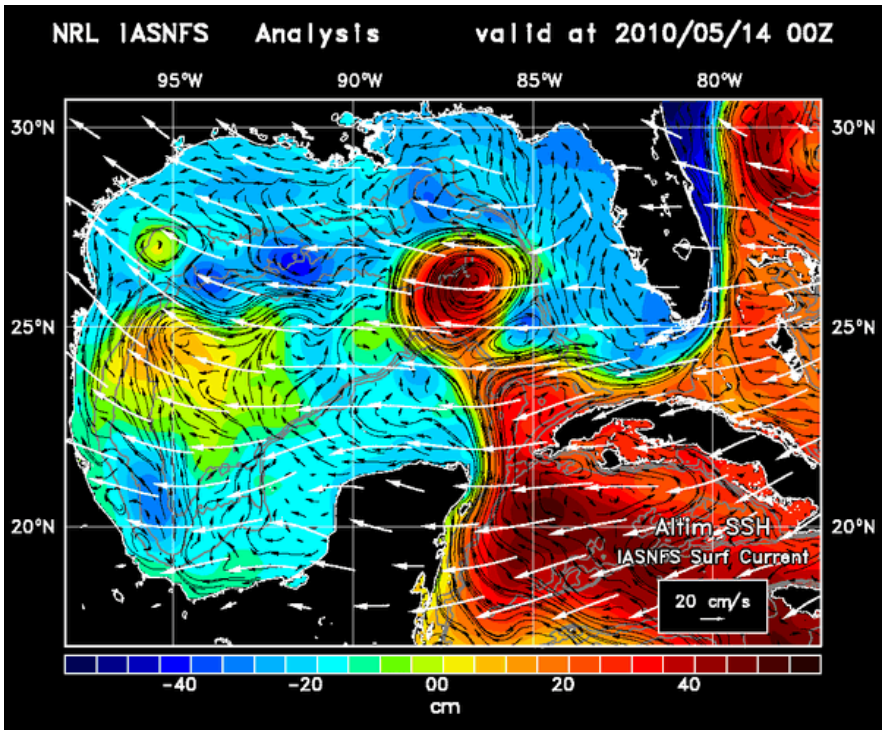

Figure 10. IASNFS reanalysis current at surface (black vectors) and NOGAPS 10 m wind (white vectors) superimposed over satellite altimeter SSH (in colors).

6 Reanalysis Product

The IASNFS reanalysis was conducted from October 1, 2001 to January 1, 2013. All model prognostic variables: temperature, salinity, current and sea surface height on the computation grid were saved except for the first 3 months during the spinup. A subset of model reanalysis was prepared for BOEM to be applied for the Oil Spill Risk Analysis model. The subset data covers the entire Gulf of Mexico and Straits of Florida from 77°W to 98°W and from 17°N to 30.7°N, as shown in Figure 10. To be readily applicable, all variables that include sea surface height, and 3D water temperature, salinity and ocean current are on the center of model grid and on the center of vertical levels. The 3D variables are at 40 depths listed in Table 2.

Table 2. Vertical depths for model 3D variables: temperature, salinity and current in the netCDF files.

Level #	Depth (m)
1	0.50
2	1.59
3	2.90
4	4.45
5	6.29
6	8.49
7	11.10
8	14.20
9	17.90
10	22.30
11	27.53
12	33.75
13	41.16
14	49.97
15	60.46
16	72.93
17	87.78
18	105.44
19	126.45
20	151.45
21	181.20
22	216.59
23	258.70
24	308.81
25	368.42
26	439.36
27	523.75
28	624.16
29	743.63

(continued)

Table 2 (Continued)

Level #	Depth (m)
30	885.78
30	885.78
31	1054.91
32	1256.14
33	1495.57
34	1780.45
35	2119.39
36	2522.67
37	3002.50
38	3573.40
39	4252.67
40	5060.87

The data set spans a period of 10 years from 00 UTC January 1, 2003 to 21 UTC December 31, 2012 with 3 h interval at 00, 03, 06, 09, 12, 18, and 21 UTC each day. In addition to the IASNFS ocean reanalysis, the 10 m wind from NOGAPS, interpolated onto the same grid, is also included in the data set.

The data were extracted from the archive and converted to BOEM approved netCDF format. A header of the netCDF file is listed in the Appendix, which provides all the essential information on the data set. To be easily transferable, the 10-year long data set, about 1.7TB in size, was separated into monthly files. Each monthly file contains data starting from 00 UTC the first day of the month and ending at 21 UTC the last day of the month. There are 120 netCDF files identified by name: iasnfs_yyyymm.nc, where "yyyy" indicates year and "mm" month.

7 Validation

Two dimensionless statistics: correlation coefficient and model efficiency or model skill are used to assess the IASNFS reanalysis against observations whenever the suitable data are available. Correlation coefficient, *Cr*, is defined as the covariance of the two variables: *x* and *y*, divided by the product of their standard deviations (Pearson, 1895):

$$Cr = \sum(x - \bar{x})(y - \bar{y}) / \left(\sqrt{\sum(x-\bar{x})^2}\ \sqrt{\sum(y-\bar{y})^2}\right).$$

Overhead bar indicates mean values. Correlation coefficient is widely used as a measure that determines the degree to which two variables' variations are associated. Applying to model evaluation, *x* is the model prediction or reanalysis and *y* is the observation. The

correlation coefficient ranges from −1 to 1. A value of 1 implies that the model describes the variation of observation perfectly. A value of 0 implies that there is no correlation between the model prediction and observation. The negative value indicates model prediction is increasing while observation is decreasing or vice versa. A correlation greater than 0.8 is generally regarded as strong, whereas a correlation less than 0.5 is generally considered as weak.

Model efficiency or model skill is also commonly used in model evaluation, and is recommended by the American Society of Civil Engineers. The model efficiency, *Skill*, is a normalized statistic that determines the relative magnitude of the model error variance compared to the measured data variance (Nash and Sutcliffe, 1970). It is defined as:

$$Skill = 1 - \sum(x - y)^2 / \sum(y - \bar{y})^2,$$

where x is model prediction or reanalysis and y is observation. Its definition is identical to the coefficient of determination, R^2, used in linear regression. Model efficiency (Skill) ranges between $-\infty$ and 1, with $Skill = 1$ corresponding to a perfect match of model prediction to the observation. An efficiency of 0 ($Skill = 0$) indicates that the model prediction is as accurate as the mean of the observed data, $\bar{y}$. An efficiency of less than zero ($Skill < 0$) occurs when the model error variance is larger than the data variance, indicating the observed mean or climatology is a better predictor than the model. Values of model efficiency between 0 and 1 are generally viewed as acceptable levels of model performance, and suggest that model has a predictive skill while the closer the value is to 1, the more accurate the model is.

7.1 Sea Surface Height

7.1.1 Satellite Altimeter Data

The IASNFS sea level reanalysis was evaluated against satellite altimeter data. Since IASNFS does not assimilate the altimeter data directly (Section 5); it is an independent data for model evaluation. The altimeter data used were the gridded SSH anomalies reanalysis produced at NAVO. As described in Section 5.1, the altimeter SSH analysis is of low frequency and long wave-length. To be more compatible in comparison, the IASNFS SSH reanalysis was filtered with 15-d Gaussian window and interpolated to altimeter 1/4° analysis grid with the 10-year mean removed. The correlation coefficient and model efficiency (skill) were calculated every 5 d and over the area shown in Figure 9 on the grids that are deeper than 1000 m. A 1000 m cutoff was applied because of the large altimeter analysis error in the shallow water (Figure 13) due to uncertainty in satellite tracking and low-signal-to-noise ratio.

The overall correlation coefficient between IASNFS prediction or reanalysis and satellite altimeter analysis, averaged over 10 years from 2003 to 2012, is 0.87 ± 0.05 (Figure 11) and the overall model efficiency (skill) is 0.65 ± 0.14 (Figure 12). Those numbers are fairly high. During the period when correlation coefficient and model efficiency are low, e.g., in January 2011 indicated by a red arrow in Figure 11, it is often caused by larger error in altimeter analysis rather than due to decline in model performance. Examining the error

maps of altimeter analysis (Figure 13), shows that relative to the normal condition (Figure 13a), the overall error during January, 2011 is quite large owing to substantial data outage (Figure 13b).

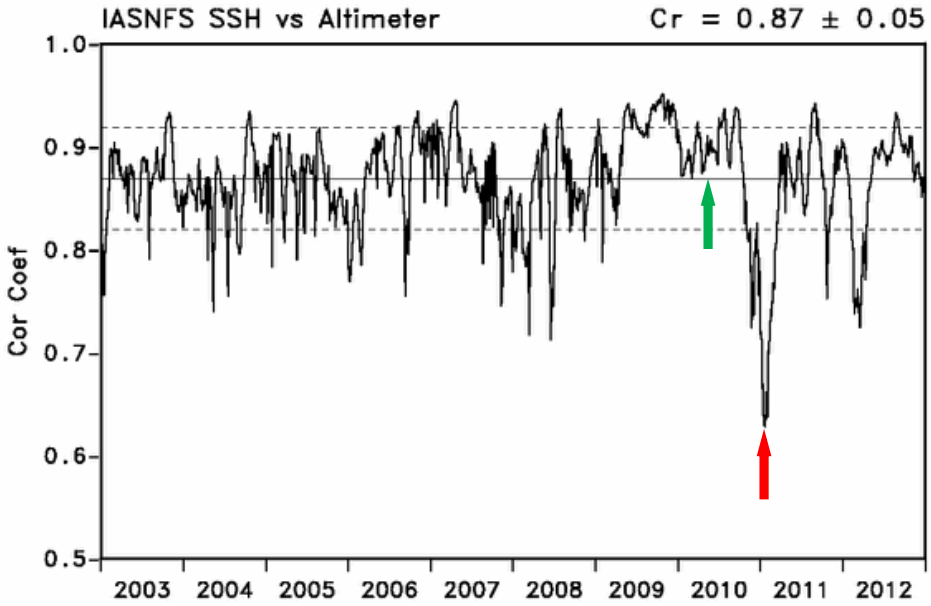

Figure 11. Correlation coefficient (Cr) for SSH anomaly between IASNFS reanalysis and altimeter analysis from 2003 to 2012 at 5 d interval. The red arrow indicates a period of low correlation coefficient.

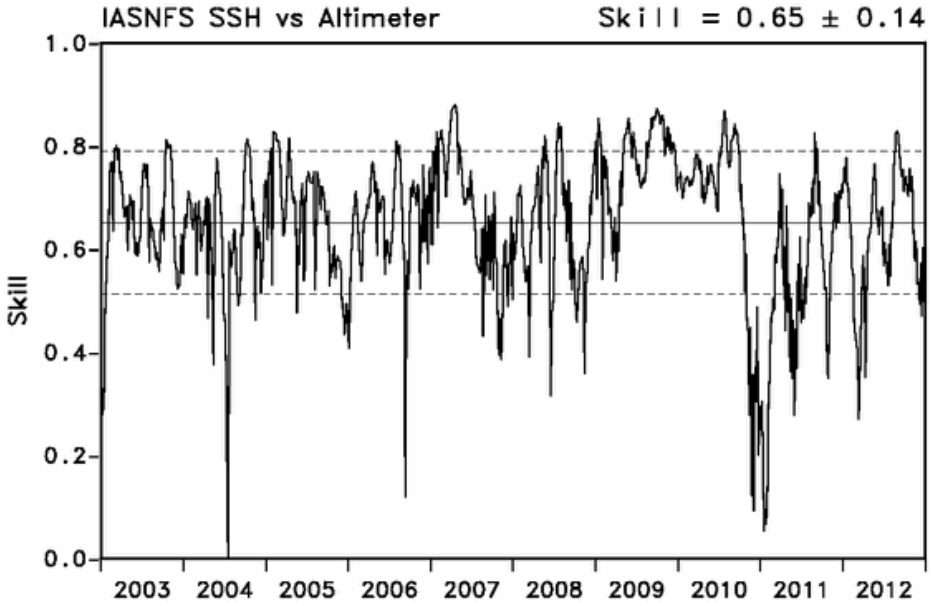

Figure 12. Model efficiency (Skill) for SSH anomaly between IASNFS reanalysis and altimeter analysis from 2003 to 2012 at 5 d intervals.

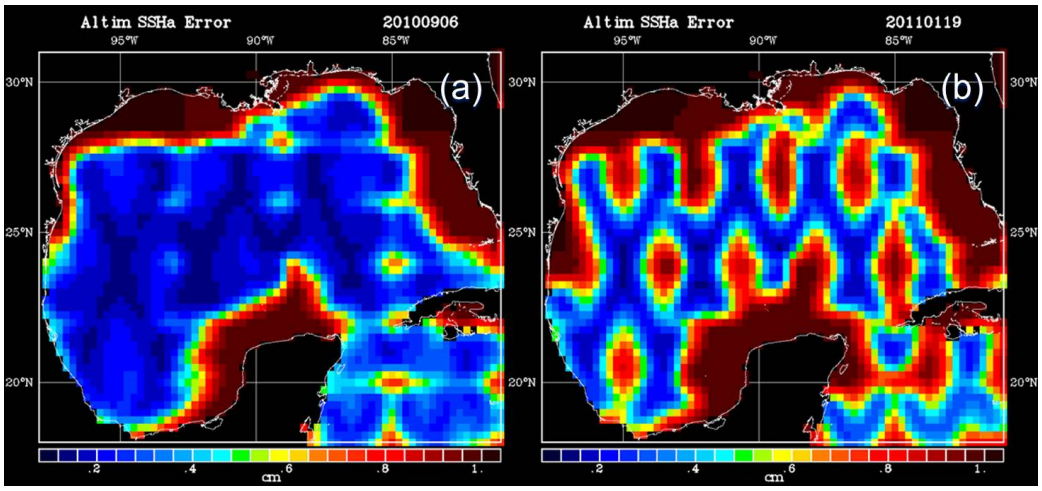

Figure 13. Error map of altimeter SSH analysis at (a) 2010/09/06 and (b) 2011/01/19. The dates are indicated by a green arrow and a red arrow respectively in Figure 11.

The satellite altimeter analysis contains mainly the SSH variations induced by the oceanic mesoscales such as boundary currents and eddies (Section 3.1). Overall high correlation coefficient (*Cr* = 0.87) between model prediction and altimeter data and model efficiency (*Skill* = 0.65) for the sea level variation indicates that IASNFS prediction (reanalysis) captured those mesoscale features very well.

7.1.2 NOS Tide Gauge Measurement

IASNFS coastal sea level reanalysis was evaluated against NOAA National Ocean Service (NOS) tide gauge measurement. The verified hourly sea level data set was obtained from NOS Center for Operational Oceanographic Products and Services (http://tidesandcurrents.noaa.gov/stations.html?type=Water+Levels) at 12 selected tidal stations along the Gulf Coast and Florida Coast as listed in Table 3. The tidal stations were selected primarily for the completeness of data set over the 10-year period but also for their evenly spaced locations along the coasts. The 3-h interval of sea level prediction in the IASNFS reanalysis was extracted at the locations of tide gauges for evaluation. Since IASNFS did not include tides for the reanalysis, the NOS tide gauge data were detided applying a 40-h Lanczos taper filter. To be consistent, IASNFS reanalysis was also subject to the same filtering and resampled at 1 h interval.

Time series of hourly subtidal sea level variations from 2003 to 2012 at all 12 tidal stations are shown in Figure 14. The 60-d low-pass filtered seasonal sea level variations are presented in Figure 15. The hourly sea level variation is rich in the synoptic scale, which is induced mainly by weather front passages and storms; the seasonal variation is equally large. There are occasional extreme high sea levels caused by the hurricane storm surges. The storm surge due to Hurricane Katrina (2005), for example, can be clearly seen in the tidal stations along the coasts of Louisiana (Grand Isle), Alabama (Dauphin Island), and Florida Panhandle (Pensacola and Apalachicola) (also see Figure 18). Small synoptic variation at

Key West, FL is likely due to its southern location that is less often visited by the weather front.

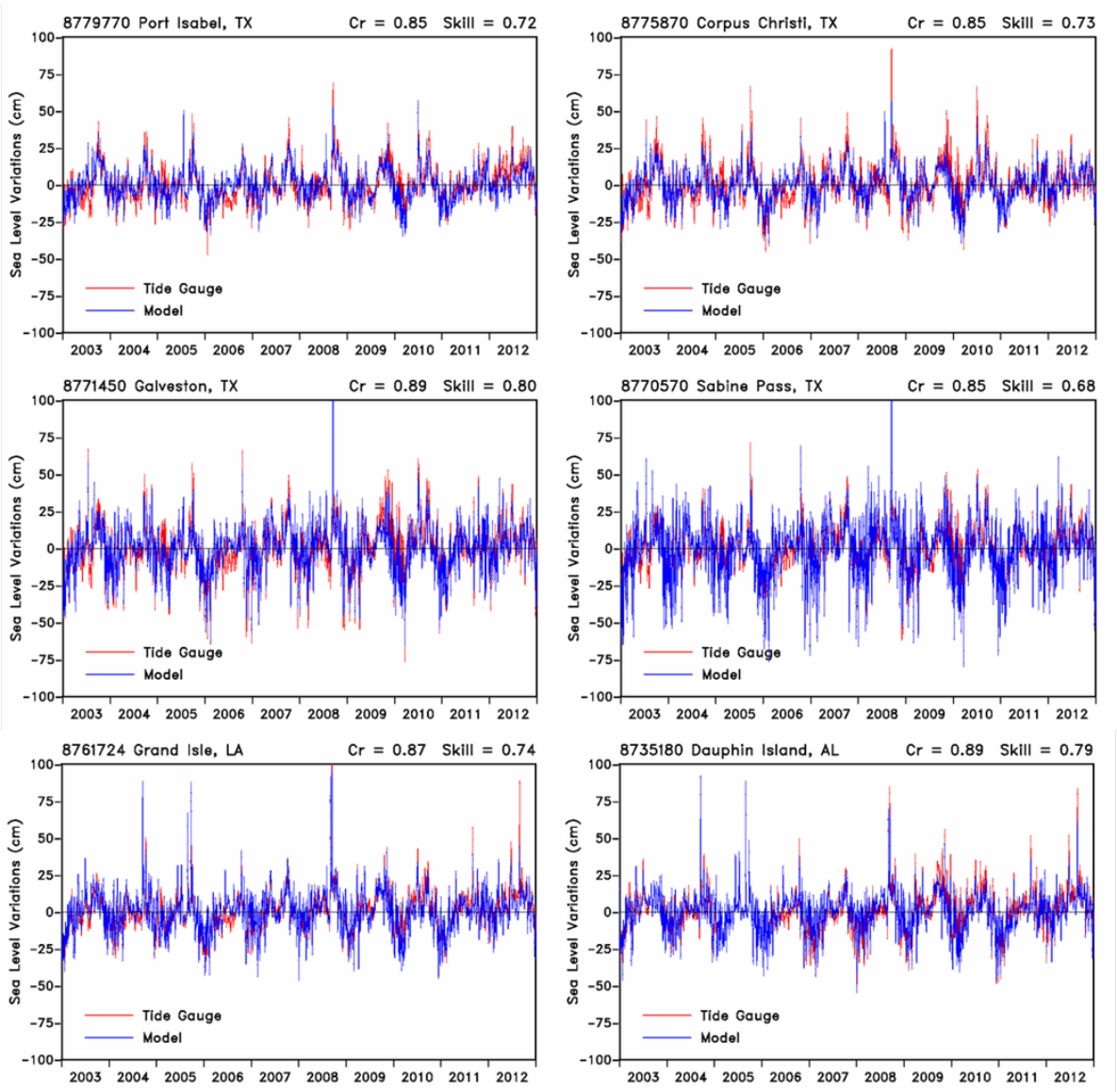

Figure 14. Time series of hourly subtidal sea level variation at NOS tidal stations across the Gulf Coast and Florida Coast as listed in Table 3. The time series was detided with a 40-h Lanczos taper filter.

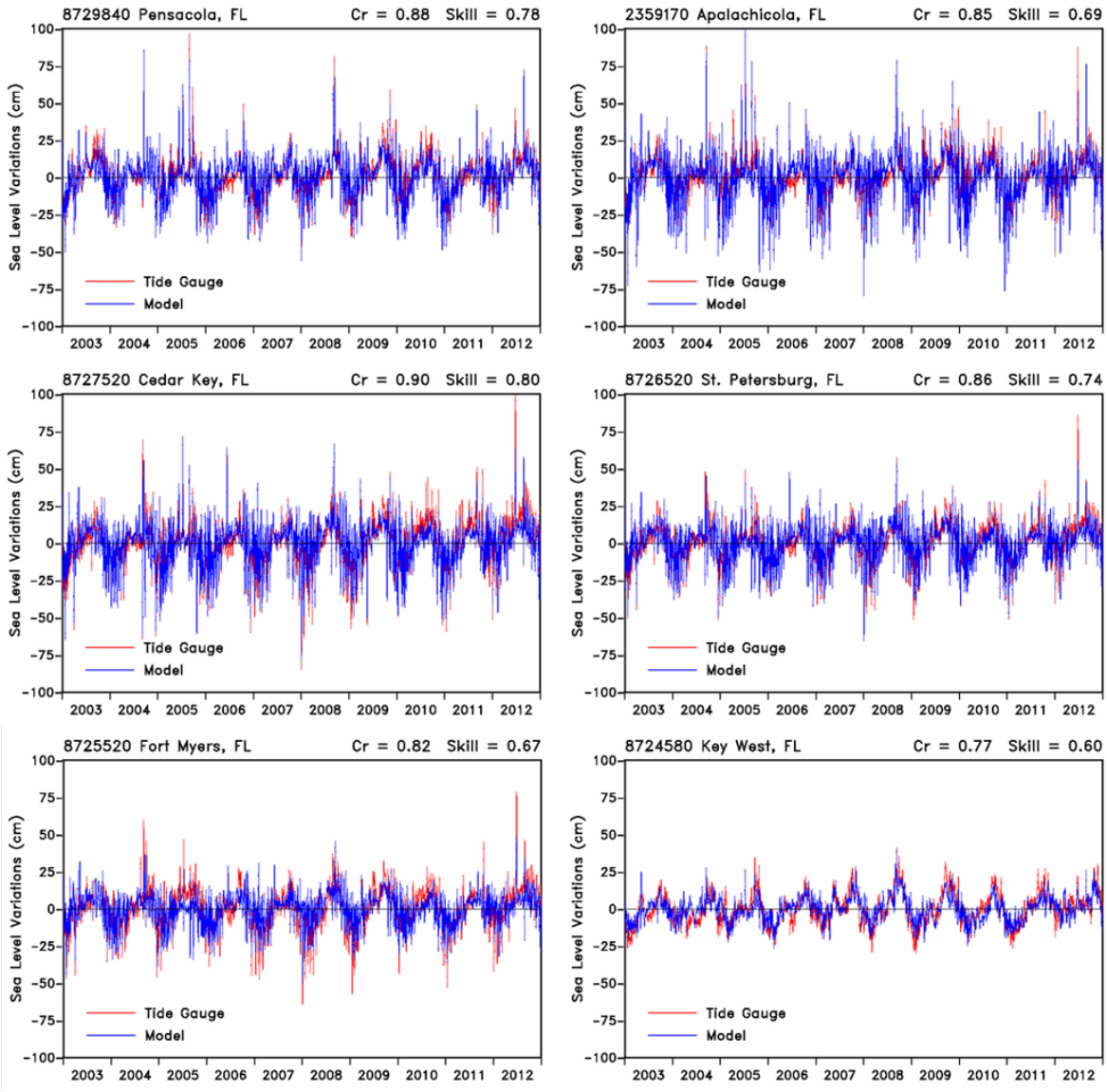

Figure 14. Continued

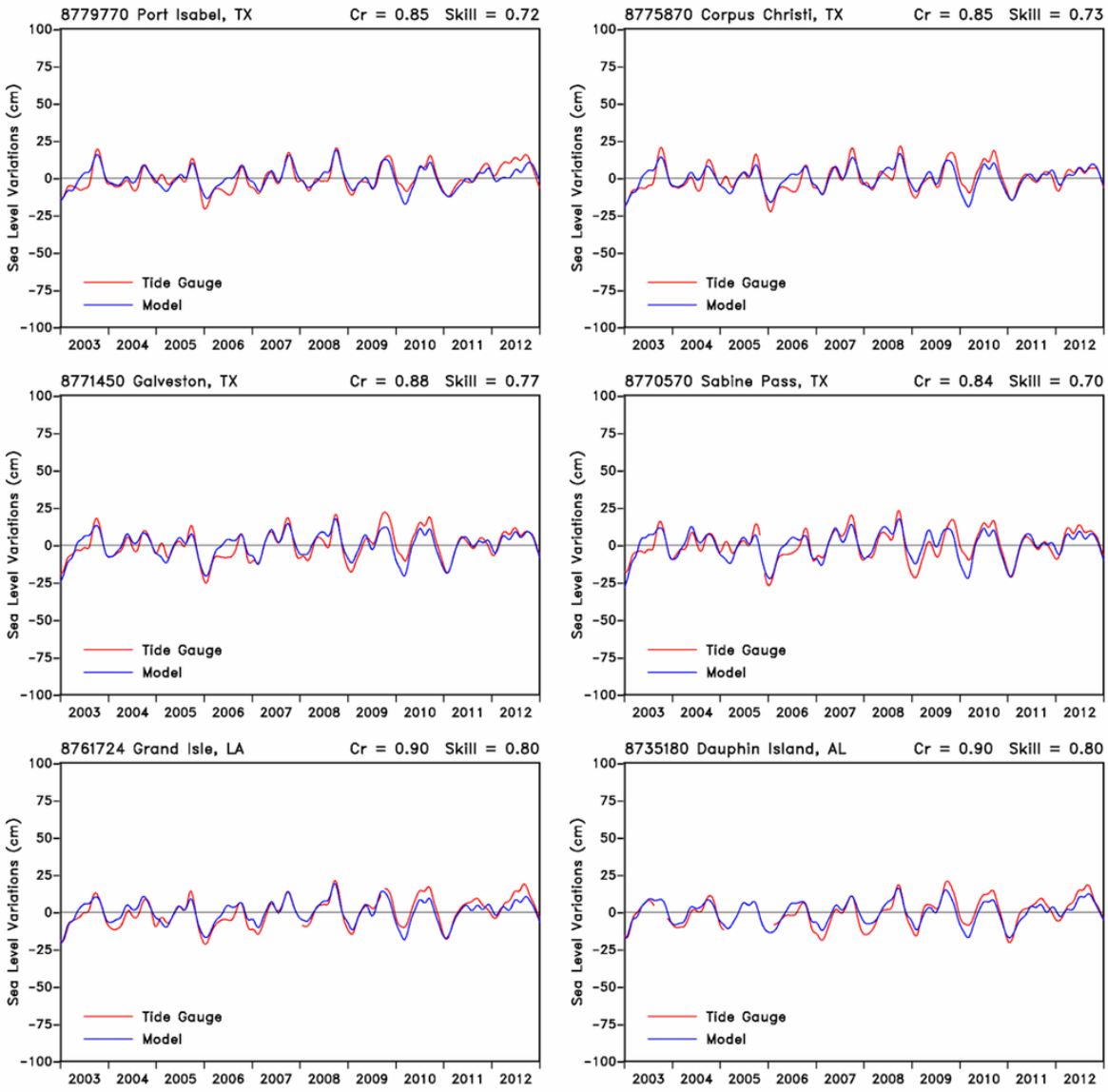

Figure 15. Time series of seasonal sea level variations at NOS tidal stations across the Gulf Coast and Florida Coast as listed in Table 3. The time series were low-pass filtered with 60-d Lanczos taper filter and resampled at 1 d intervals.

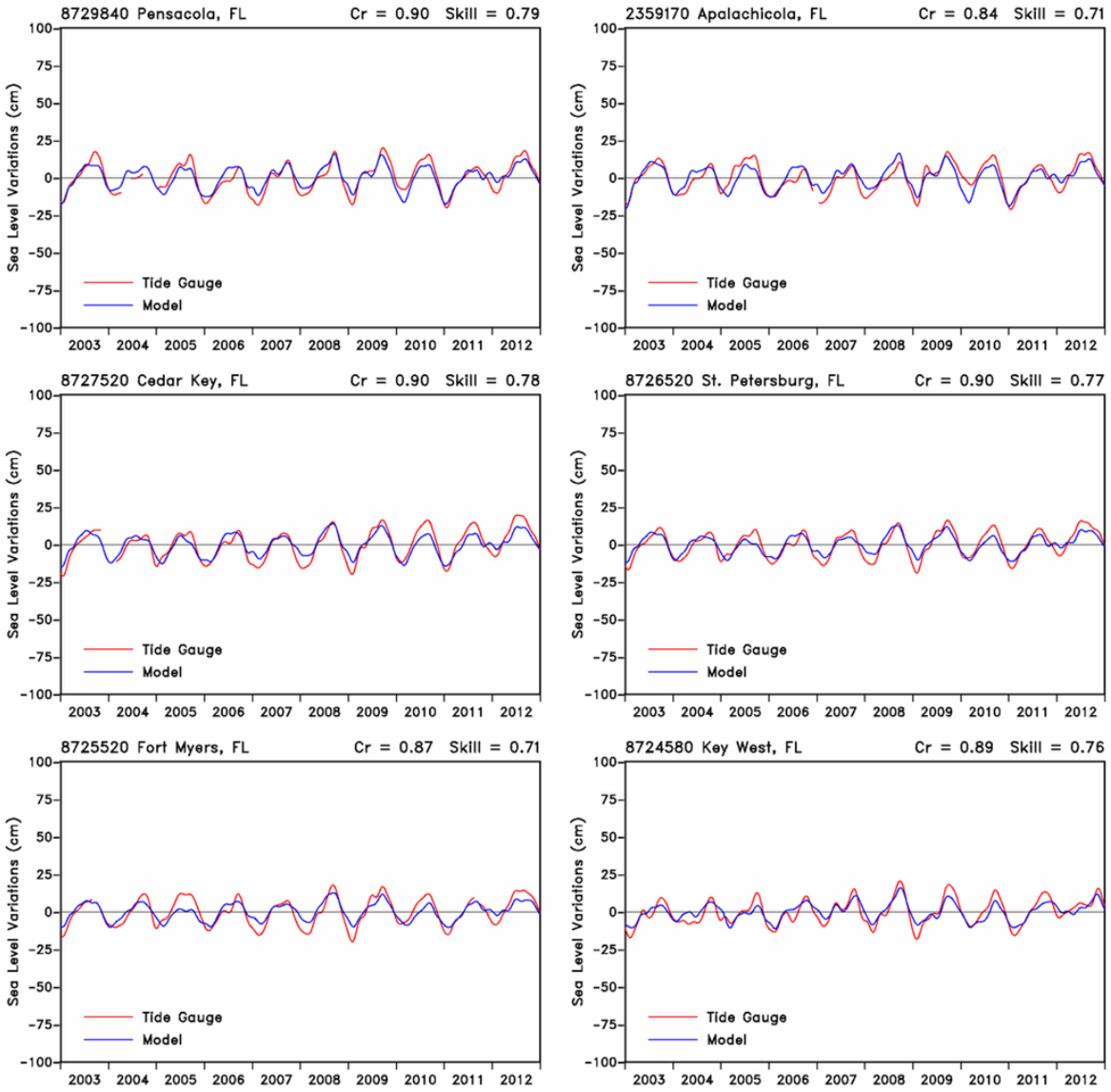

Figure 15. Continued

The correlation coefficients between IASNFS reanalysis and tide gauge data (Figure 16) and model efficiencies (skills) (Figure 17) are plotted on the map at the locations of NOS tidal stations and listed in Table 3. The correlation coefficients for all stations are quite high ($Cr \geq 0.82$) except for Key West, FL ($Cr = 0.77$). The islet where Key West is located is ill-represented in the model due to grid resolution. Also, Key West is surrounded by open oceans, where waters are free to move as compared to the other stations that are located on and constrained by the coast. Therefore, its short-time sea level variations are more difficult for the model to predict.

The model efficiency (skill) ranges from 0.60 at Key West to 0.80 at Galveston, TX and Cedar Key, FL (Table 3). In addition to Key West, a few stations that show lower model skill, although still very high, are located either in a waterway several miles from the ocean,

such as at Sabine Pass, TX (*Skill* = 0.68) and Fort Myers, FL (*Skill* = 0.67), or inside a semi-enclosed shallow bay, such as at Apalachicola, FL (*Skill* = 0.69). Those geographic features cannot be resolved by the model. The sea levels at those locations were taken from the nearest model ocean grid. That factor may have impact on the correlation and model skill.

The subtidal coastal sea level variation is mainly driven by the wind and to a lesser extent by sea level air pressure variation. The high correlation coefficient between IASNFS reanalysis and tide gauge measurement and the high model skill to predict sea level variation suggest that the NOGAPS wind forcing (Section 4) applied for the reanalysis is fairly accurate and the model responded to the wind forcing quite well.

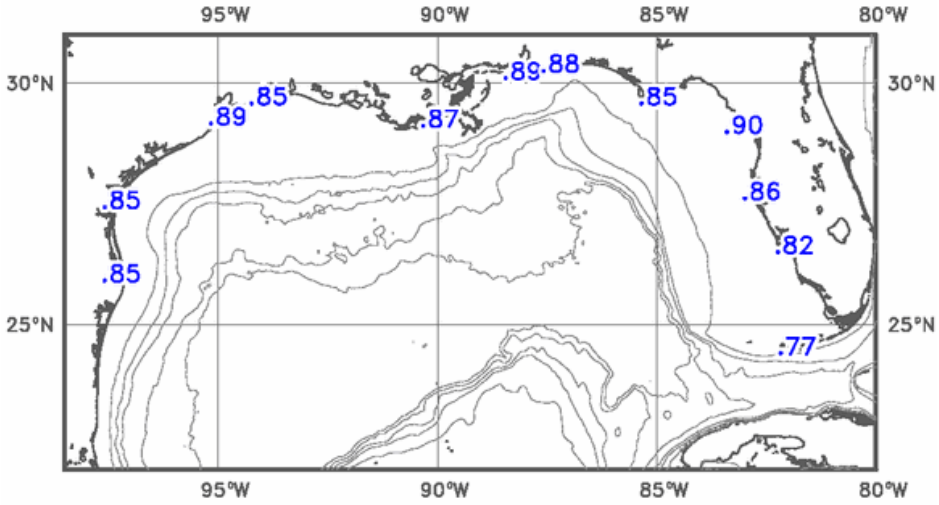

Figure 16. Map of correlation coefficient of coastal sea level variation between detided NOS tide gauge measurement and IASNFS reanalysis. The tide stations from west to east along the coast are Port Isabel, TX, Corpus Christi, TX, Galveston, TX, Sabine Pass, TX Grand Isle, LA, Dauphin Island, AL, Pensacola, FL, Apalachicola, FL, Cedar Key, FL, St. Petersburg, FL, Fort Myers, FL, and Key West, FL.

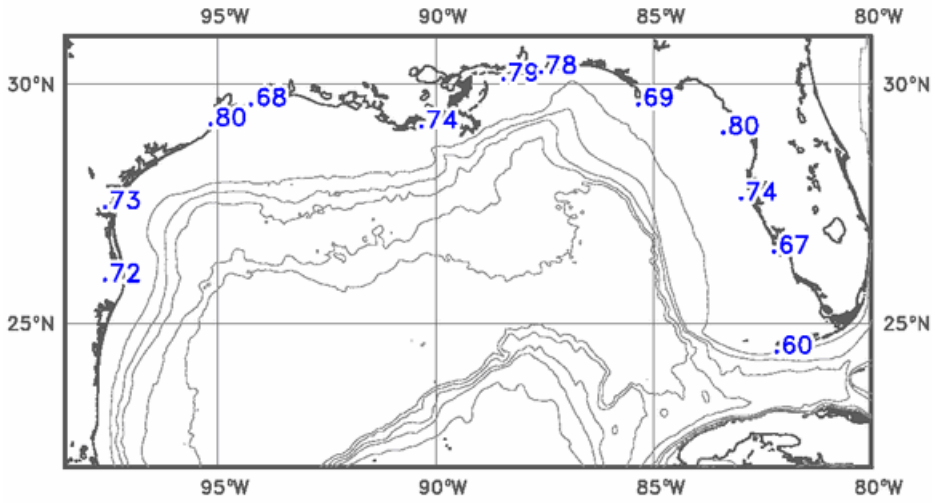

Figure 17. Map of model efficiency (Skill) evaluated against NOS tide gauge sea level measurement.

Table 3. List of correlation coefficient between tide gauge measurement and IASNFS sea level reanalysis and model efficiency (skill) at selected NOS tide stations along the Gulf Coast and Florida Coast in the Gulf of Mexico.

NOS Station ID	Location	Correlation Coef.	Model Skill
8779770	Port Isabel, TX	0.85	0.72
8775870	Corpus Christi, TX	0.85	0.73
8771450	Galveston, TX	0.89	0.80
8770570	Sabine Pass, TX	0.85	0.68
8761724	Grand Isle, LA	0.87	0.74
8735180	Dauphin Island, AL	0.89	0.79
8729840	Pensacola, FL	0.88	0.78
2359170	Apalachicola, FL	0.85	0.69
8727520	Cedar Key, FL	0.90	0.80
8726520	St. Petersburg, FL	0.86	0.74
8725110	Fort Myers, FL	0.82	0.67
8724580	Key West, FL	0.77	0.60

The accuracy of NOGAPS wind forcing and model sea level response can be further demonstrated in the storm surge during 2005 Hurricane Katrina. Figure 18 shows sea level measurement without filtering (in red curve) at Waveland, MS, located right on the track of Karina, before the station was overwhelmed by the storm surge. The IASNFS (in blue curve) predicted the arrival time of surge precisely, though the range of the predicted storm surge was lower than the estimated. It indicates that the NOGAPS is quite accurate in the time

being of the hurricane if not in intensity because of coarse resolution. It also shows the IASNFS responses to strong wind very well even during an intense hurricane.

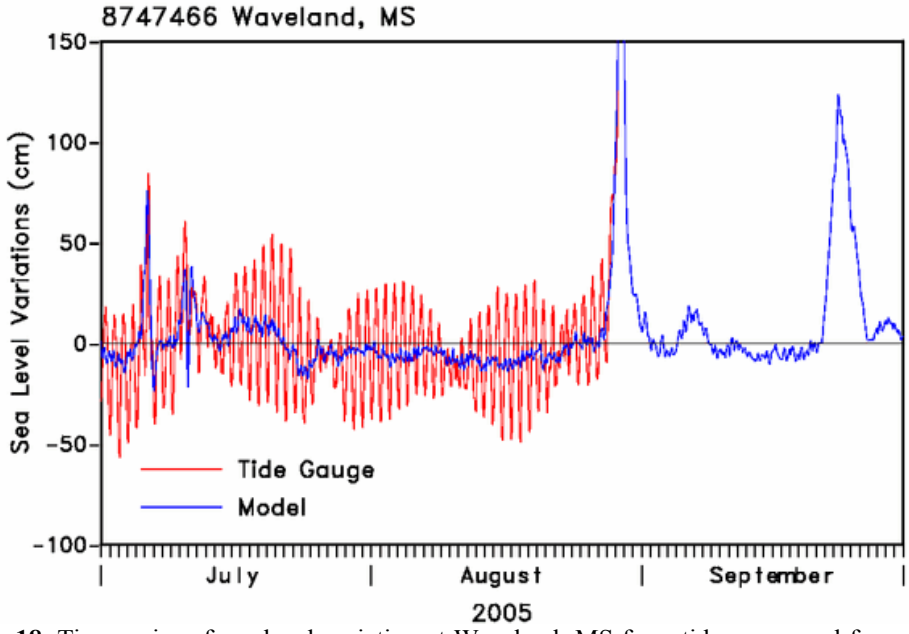

Figure 18. Time series of sea level variation at Waveland, MS from tide gauge and from IASNFS prediction (without tide) for the summer 2005. The tidal station at Waveland was on the track of Hurricane Katrina and was destroyed by the storm surge (August 29). The second storm surge in the late September was induced by Hurricane Rita.

The seasonal sea level variation (Figure 15) mainly reflects the seasonal shift in the large scale wind and air pressure pattern, it cannot be fully produced by the limited domain IASNFS. The seasonal signal was generated in the Global NCOM and conveyed into IASNFS via open boundaries. The good match between prediction and measurement ($Cr \geq 0.84$) in the seasonal scale sea level variation inside the IASNFS domain shows the effectiveness of boundary conditions that were applied in IASNFS (Section 3.3). The Global NCOM was forced with NOGAPS wind; it suggests NOGAPS wind is accurate at the seasonal scale as well.

7.2 Sea Surface Temperature

7.2.1 National Data Buoy Center Buoy Measurement

The IASNFS SST reanalysis was evaluated against the NOAA National Data Buoy Center (NDBC) (http://www.ndbc.noaa.gov/) buoy measurement. Eleven NOAA operational buoys in the Gulf of Mexico and one at Yucatan Basin in the Caribbean Sea (Figure 20) that have long-term measurements during 2003-2012 were selected. Those 12 buoys cover all ocean topographic regimes from shallow water to deep basins. Five buoys (Buoy ID: 42001, 42002, 42003, 42055 and 52056) are located in the deep water, 6 buoys (42007, 42012, 42019, 42020, 42035 and 42036) on the continental shelf, some are fairly near shore or at the shelf break, and 2 buoys (42040 and 42039) are over the continental slope. The data

used is the hourly sea surface temperature, referred to as the hull temperature which is a measure of average 1 m below surface. The IASNFS SST reanalysis was sampled at the buoy locations for evaluation. IASNFS reanalysis are 3 hourly, and the buoy data were resampled at every 3 h.

The time series of sea surface temperatures from buoys and from IASNFS between 2003 and 2012 at all 12 buoy locations are shown in Figure 19. The SST has strong synoptic scale variation induced by the passage of weather fronts during the winter and tropic storms during the summer. The seasonal variation nevertheless is much larger, responding to the substantial seasonal cooling and warming in the region.

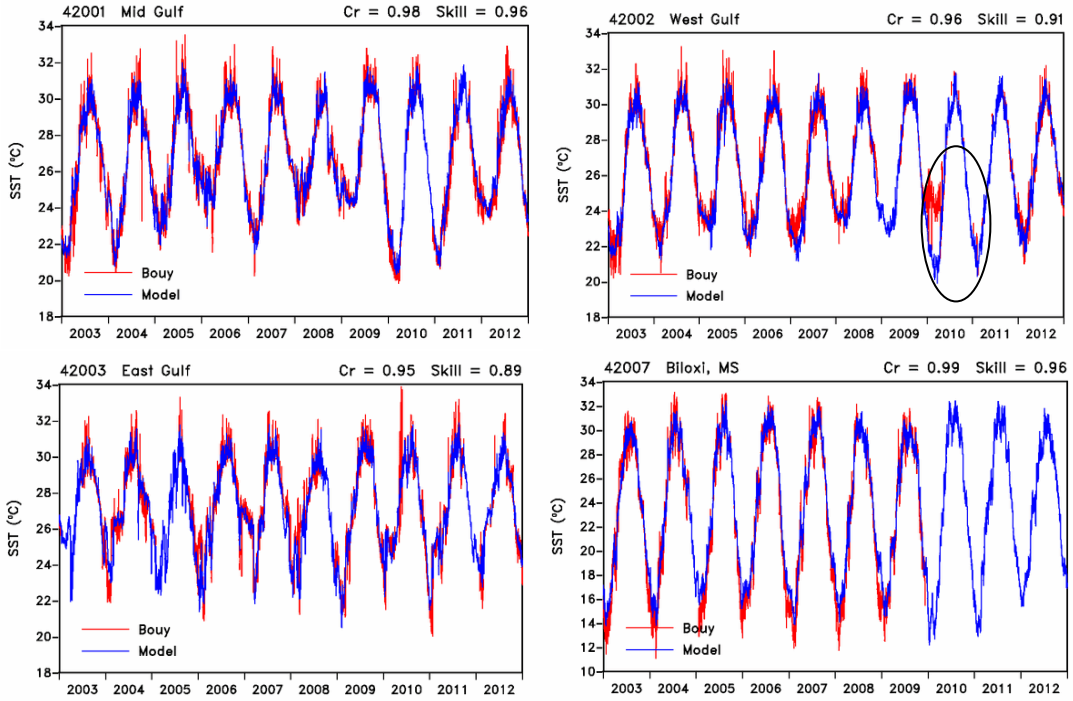

Figure 19. Time series of sea surface temperature from buoys (in red) and from IASNFS reanalysis (in blue). The NDBC buoy locations are shown in Figure 20. The bad data at buoy 42002 (West Gulf) is circled in black ellipse. Note that several buoys have substantial missing data.

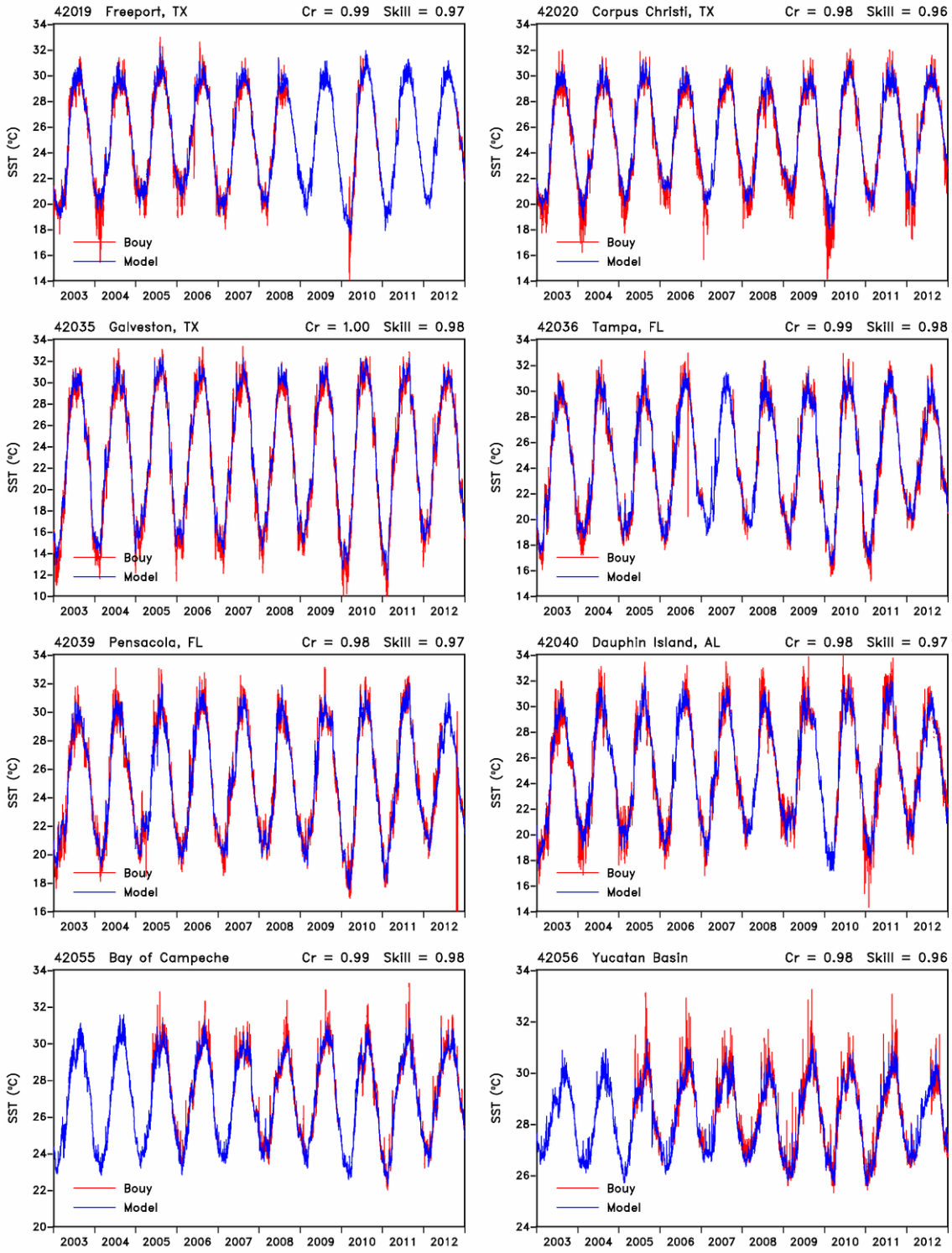

Figure 19. Continued.

The quality of buoy measurements is not very good. There are a few outliners that can be clearly identified from the time series in Figure 19. Substantial data outages also exist in the

measurements, likely due to prolonged instrumentation failure. For the buoys at Bay of Campeche (42055) and Yucatan Basin (42056), the measurement did not begin until 2005. During early months of 2010, the temperature measurement is suspiciously high at West Gulf (Buoy 42002, Figure 19). Compared to MCSST in Figure 22, it is clear that the measurement is in error. This is the time of the Deep Water Horizon incident. All NOAA ships in the region were in response to the oil spill so there was no ship to maintain the buoys. The overly high temperature in the buoy measurement is likely caused by instrument failure.

There was no intention to correct those erroneous measurements for the model evaluation.

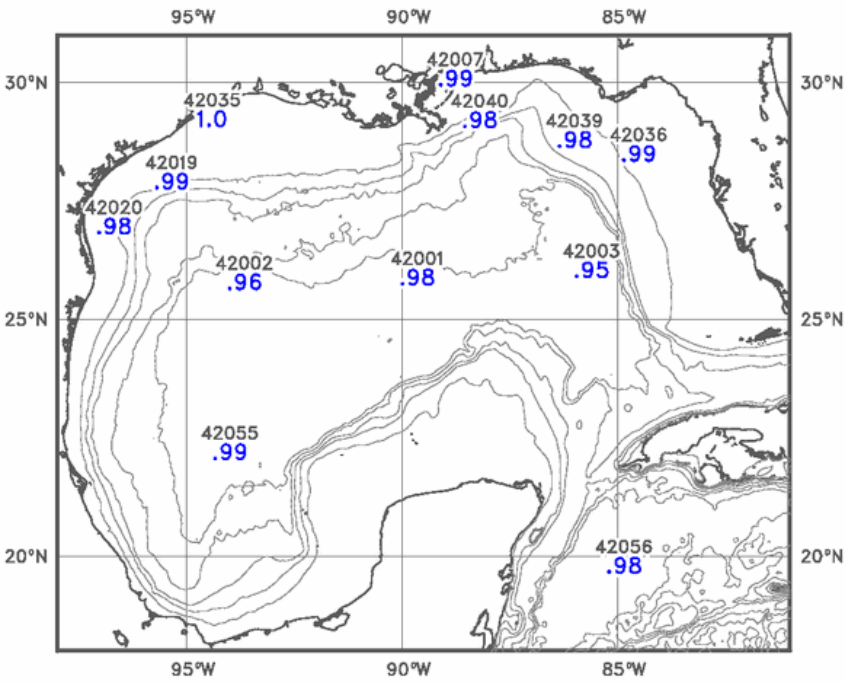

Figure 20. Map of correlation coefficient of sea surface temperature (in blue) between NDBC buoy measurements and IASNFS reanalysis. The NDBC buoy ID is indicated.

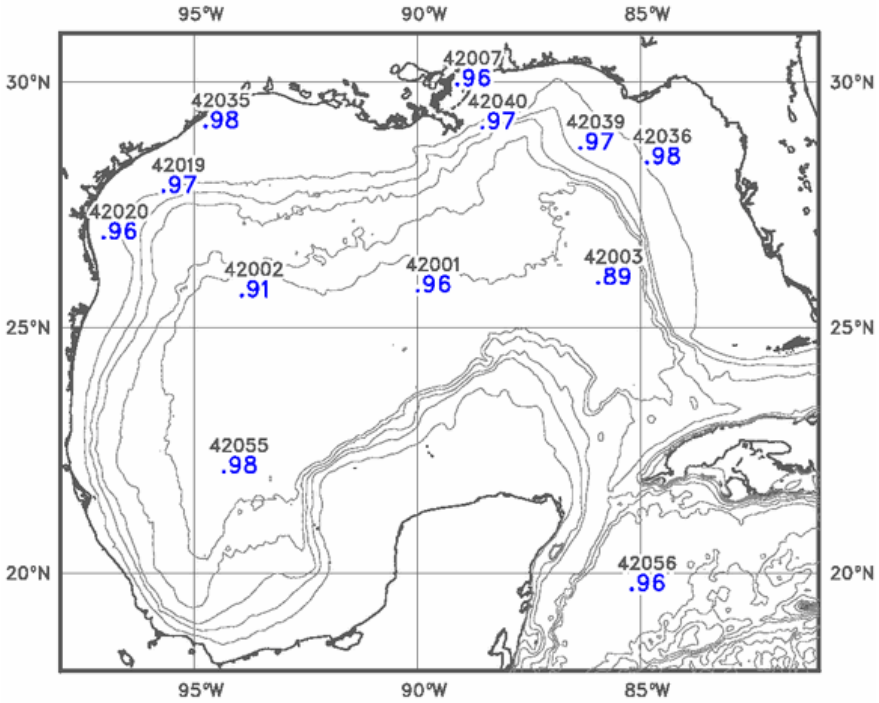

Figure 21. Map of model efficiency (skill) for the sea surface temperature (in blue) evaluated against NDBC buoy measurement.

The correlation coefficients (Figure 20) for the SST between IASNFS reanalysis and buoy measurement and model efficiencies (skills) (Figure 21) are plotted on the map at each buoy location and listed in Table 4. Despite some errors in the buoy measurements, the correlation coefficients are very high ($Cr \geq 0.95$) for all locations. The model efficiencies are also very high ($Skill \geq 0.89$). Relatively few bad data points from buoys seem to have not contaminated the statistics.

Table 4. List of correlation coefficients between tide gauge measurements and IASNFS reanalysis and model efficiency (skill) for sea surface temperature at the selected NDBC locations in the Gulf of Mexico and the Caribbean Sea

NDBC Buoy ID	Location	Correlation Coef.	Model Skill
42001	Mid Gulf	0.98	0.96
42002	West Gulf	0.96	0.91
42003	East Gulf	0.95	0.89
42007	Biloxi, MS	0.99	0.96
42019	Freeport, TX	0.99	0.97
42020	Corpus Christi, TX	0.98	0.96
42035	Galveston, TX	1.00	0.98

NDBC Buoy ID	Location	Correlation Coef.	Model Skill
42036	Tampa, FL	0.99	0.98
42039	Pensacola, FL	0.98	0.97
42040	Dauphin Island, AL	0.98	0.97
42055	Bay of Campeche	0.99	0.98
42056	Yucatan Basin	0.98	0.96

The overall high correlation and model skill in the SST is understandable. The SST in the region is dominated by seasonal variations that are several times larger than the synoptic scale. The model tends to predict seasonal variations better than the synoptic scale, simply because the atmospheric forcing applied to drive the model is more accurate in the seasonal scale than in the synoptic scale.

The slightly lower correlation coefficient (*Cr* = 0.96) and model skill (*Skill* = 0.91) at West Gulf (Buoy 42002) is mostly due to a period of poor measurement (Figure 19) discussed earlier. At East Gulf (Buoy 42003), the correlation coefficient (*Cr* = 0.95) and model skill (*Skill* = 0.89), although still very high, are the lowest among the 12 selected buoy locations. This buoy is located at a region where it is regularly visited by the Loop Current and Loop Current Eddies. IASNFS may not predict precisely those strong mesoscale features, in particular, the smaller scale frontal eddies. This would result in slightly lower correlation and model skill.

7.2.2 Satellite MCSST

The IASNFS sea surface temperature reanalysis was evaluated against the satellite MCSST. The MCSST data used are the reanalysis on 1/8° grid produced in daily interval at NAVO (Section 5.1.2). Satellite MCSST was used to adjust the NOGAPS heat flux for model forcing (Section 4) and, together with satellite altimeter data, was utilized by MODAS to produce the temperature analysis for the data assimilation. Since the vertical weighting function applied for data assimilation is 0 at the sea surface (Section 5.2), MCSST is not (directly) assimilated. MCSST is therefore an independent data set for model evaluation.

To be comparable to the evaluation against buoy measurements (Section 7.2.1), 12 sets of time series were created by sampling the daily MCSST reanalysis at the same buoy locations that are shown in Figure 20. As described in Section 5.1.2, the MCSST analysis is a 5-d composite. To be consistent, the IASNFS SST reanalysis was low-pass filtered with 5-d Lanczos taper filter and resampled at 24 h for comparison.

Time series graphs of sea surface temperatures from MCSST and from IASNFS at all 12 buoy locations are shown in Figure 22. The MCSST analysis is basically a 5-d average, it has much-reduced synoptic scale variations compared to buoy measurements (Figure 19), but it retains the seasonal scale variation. At all locations, IASNFS SST reanalysis follows the MCSST very well. The overly high temperature in the buoy measurement (42002) during 2010 Deep Horizon oil spill does not exist in the MCSST.

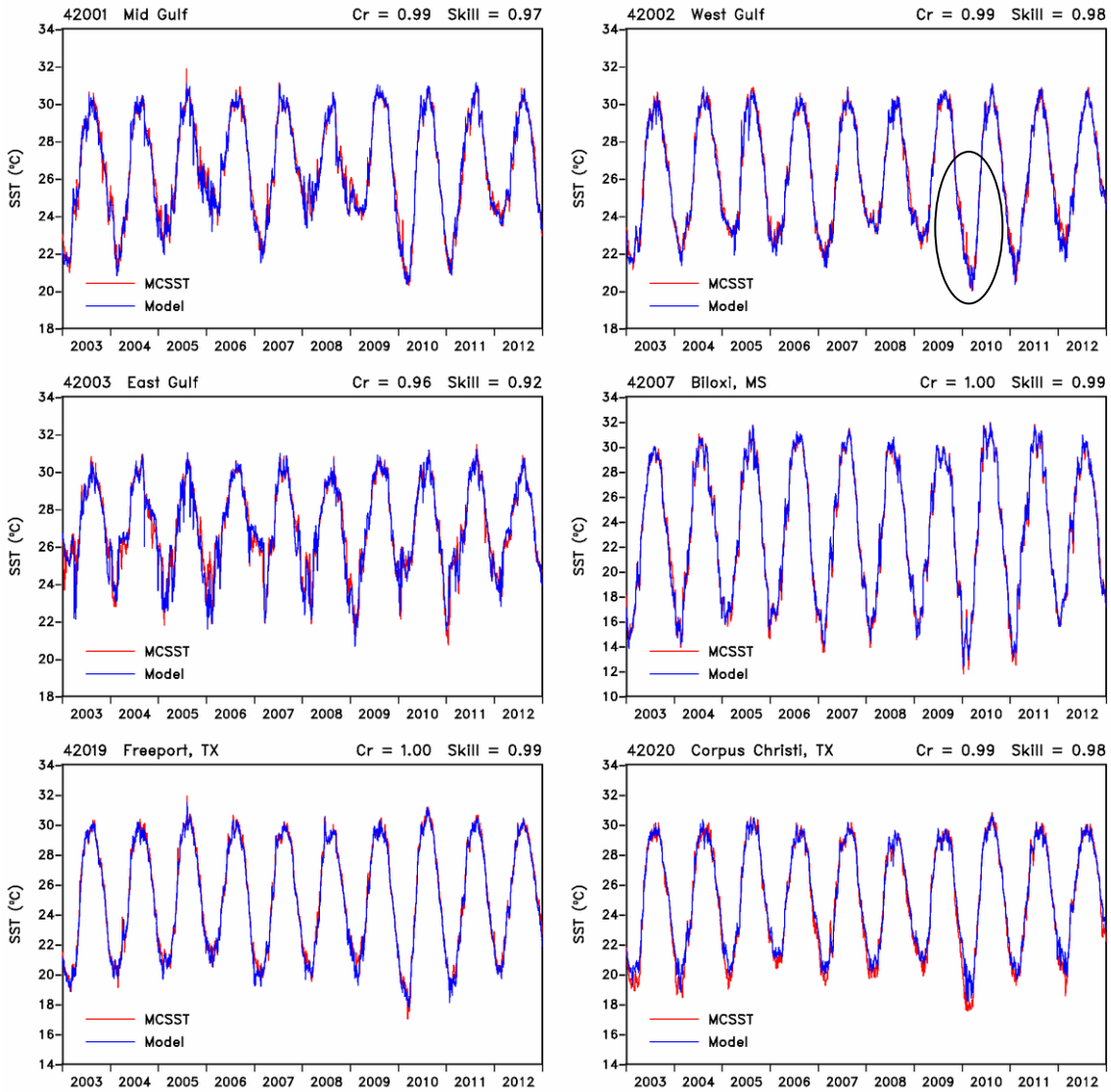

Figure 22. Time series of sea surface temperature from MCSST (in red) and from IASNFS reanalysis (in blue) at NDBC buoy locations shown in Figure 20.

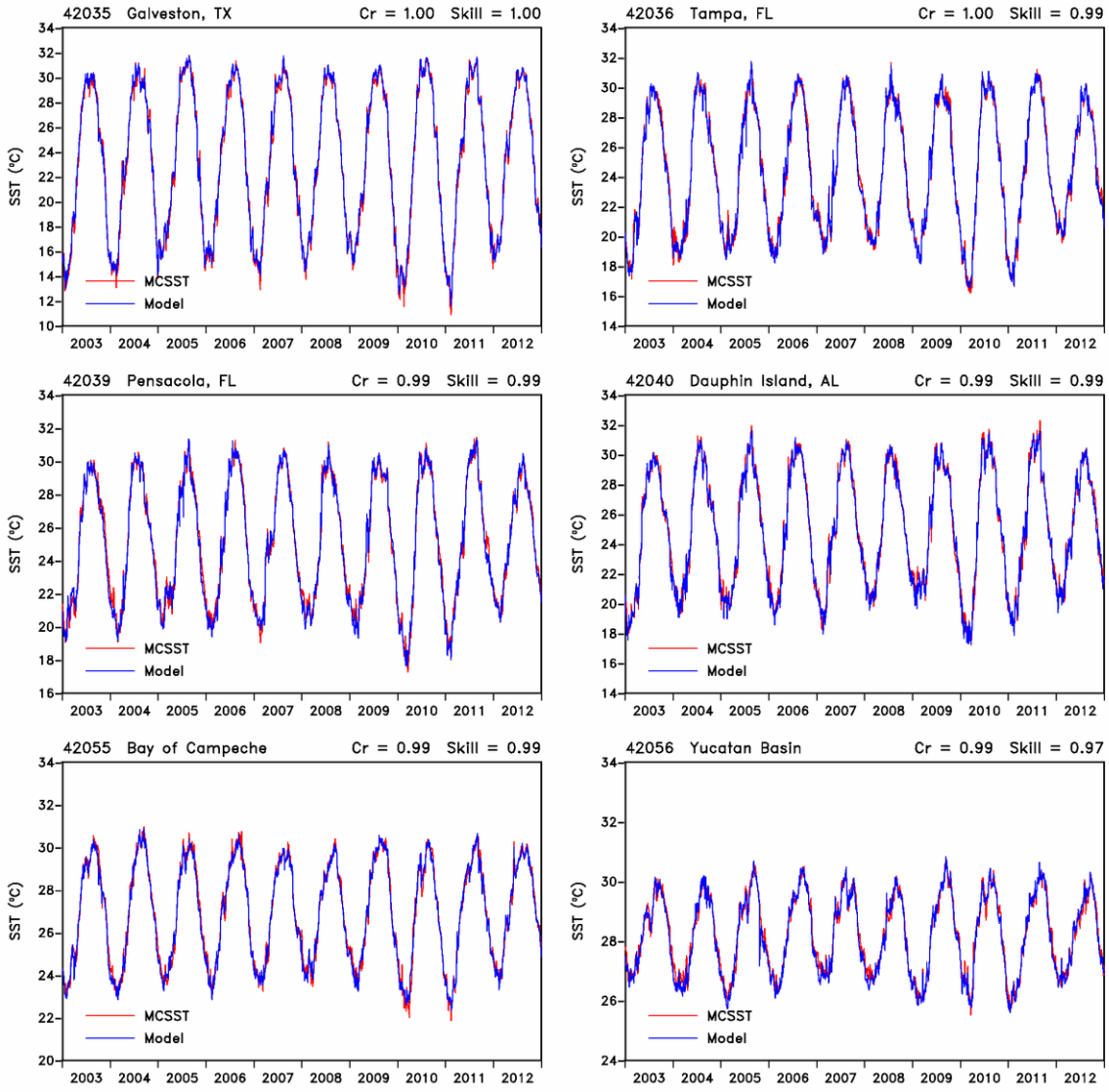

Figure 22. Continued.

The correlation coefficients (Figure 23) between IASNFS SST reanalysis and MCSST and the model efficiencies (skills) (Figure 24) are plotted on the map at buoy locations and listed in Table 5. The correlation coefficients are extremely high ($Cr \geq 0.96$) for all locations. The model efficiencies are also very high ($Skill \geq 0.92$). Slightly lower numbers ($Cr = 0.96$ and $Skill = 0.92$) at the buoy (42003) located at East Gulf is due to complex mesoscale activities that model may not predict precisely. Overall high numbers (Table 5), higher than those evaluated against buoy measurements (Table 4), are because the evaluation was done using 5-d filtered data in which the synoptic scale variation from atmospheric forcing has been more or less removed. The comparison is dominated by the seasonal scale that the model predicts very well.

The overall high correlation and model skill for the IASNFS SST reanalysis evaluated against both NDBC buoy measurements and MCSST suggest that the NOGAPS surface heat flux is adequate and the scheme (Sections 4) employed for heat forcing by IASNFS is robust.

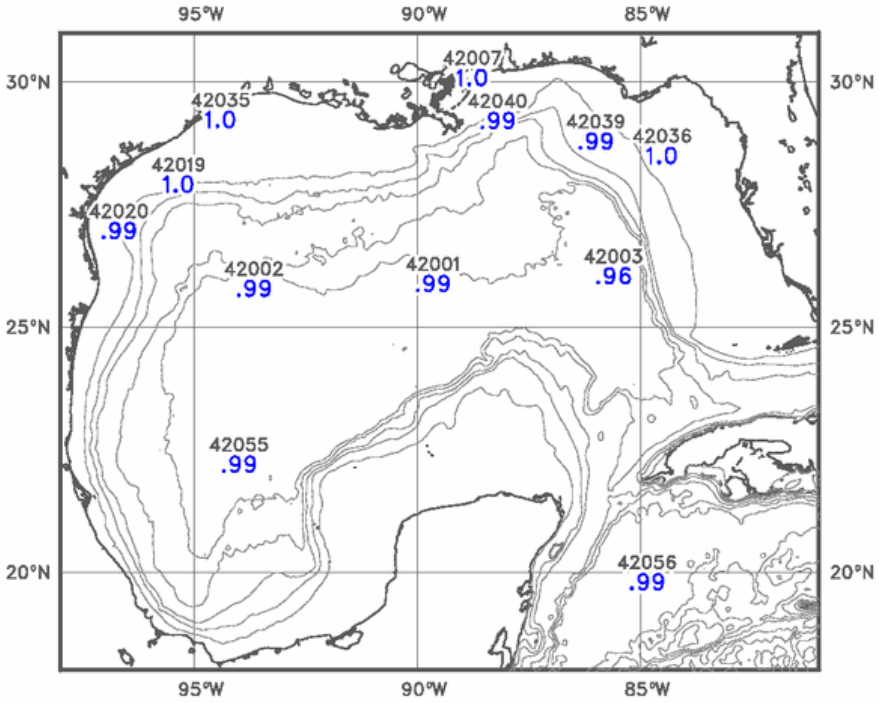

Figure 23. Map of correlation coefficient of sea surface temperature (in blue) between MCSST and IASNFS reanalysis at NDBC buoy locations.

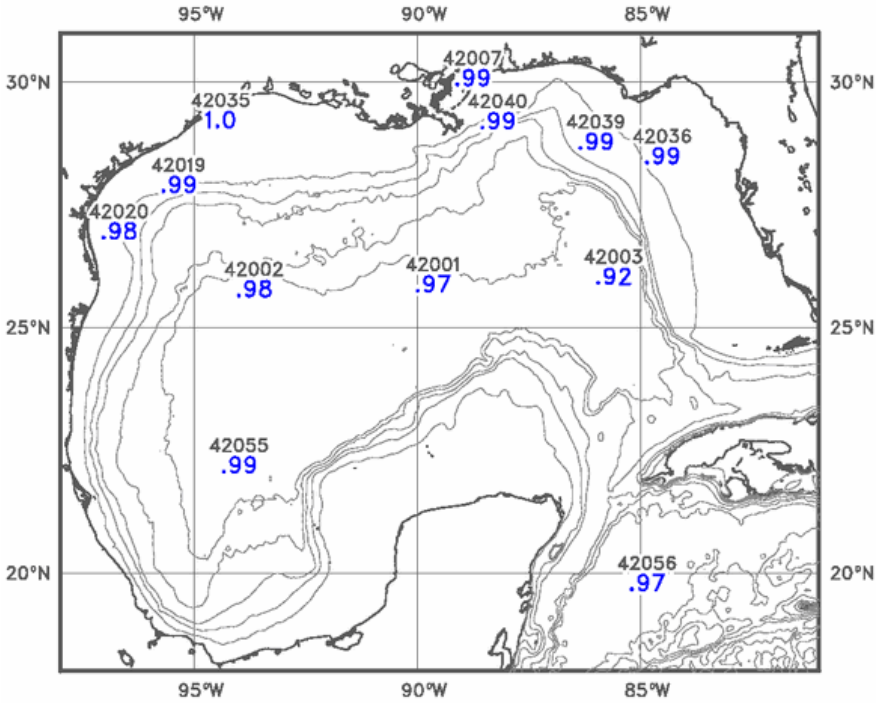

Figure 24. Map of model efficiency (skill) for the sea surface temperature (in blue) evaluated against MCSST.

Table 5. List of correlation coefficient and model efficiency (skill) against MCSST at the selected NDBC locations in the Gulf of Mexico and the Caribbean Sea

NDBC Buoy ID	Location	Correlation Coef.	Model Skill
42001	Mid Gulf	0.99	0.97
42002	West Gulf	0.99	0.98
42003	East Gulf	0.96	0.92
42007	Biloxi, MS	1.00	0.99
42019	Freeport, TX	1.00	0.99
42020	Corpus Christi, TX	0.99	0.98
42035	Galveston, TX	1.00	1.00
42036	Tampa, FL	1.00	0.99
42039	Pensacola, FL	0.99	0.99
42040	Dauphin Island, AL	0.99	0.99
42055	Bay of Campeche	0.99	0.99
42056	Yucatan Basin	0.99	0.97

7.3 Ocean Current

The IASNFS ocean current reanalysis was evaluated against the mooring measurements. Since processing of current meter data is beyond the scope of this report, the evaluation was limited to a qualitative comparison to demonstrate model's utility. Specifically, we compared the Eddy Franklin event of March - July, 2010, which was captured by an array of intense current meter moorings during the BOEM-sponsored Loop Current Dynamics Study (Hamilton, P., 2013). The locations of moorings are shown in Figure 25.

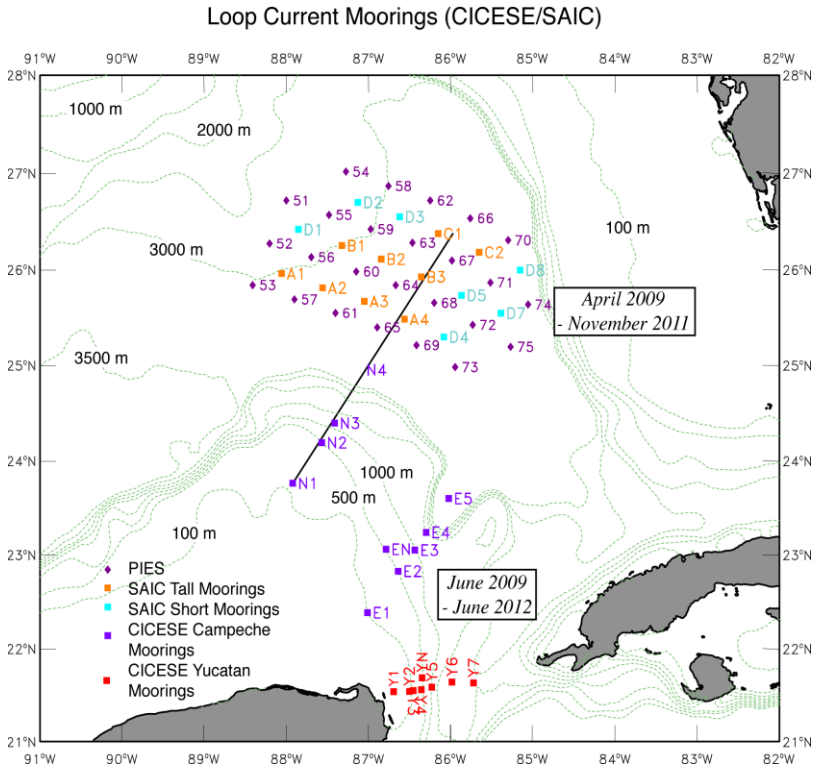

Figure 25. Locations of moorings for the Loop Current Dynamics Array and the Ensenada Center for Scientific Research and Higher Education's Arrays.

The daily averaged IASNFS near-surface currents at 80 m was interpolated to the mooring locations. Figure 26, on the right column, shows a sequence of model-predicted surface currents and sea surface anomalies of Eddy Franklin every 15 days from March 1, 2010 to July 14, 2010. On the left column, it shows the corresponding observed surface currents and sea surface anomalies (Hamilton, P., 2013). We note that the 'observed' SSH boundary was interpolated from the rather coarse 1/4° (cross track spacing = 285 km for the TOPEX/Poseidon (T/P) and Jason altimeter satellites) altimetry SSH analysis provided by B.

Lebon of University of Colorado, and lacked the detailed structure found in the model. The altimeter analysis may also incur large error from data outage as discussed in Section 5.1.1.

By March 1, the Loop Current already had extended quite far north to about 27°N from its nominal position of about 24°N. The model and observations are in very good agreement up to the end of April. Their spatial patterns are basically the same. Perhaps most encouragingly, the model currents at individual moorings inside the region shown in Figure 26 are also comparable to the observations. We note that the model did not assimilate any data from the Loop Current Dynamics Study.

The model eddy was separated from the Loop Current on May 15. The observed SSH based on the altimeter analysis were not able to fully resolve the Loop Current eddy separation due to its coarse resolution. The dense mooring array, on the other hand, missed the critical coverage south of 25°N where the eddy breakup took place. Nevertheless, consistent with the model result, the observed currents indicated a rapid change of flow pattern between April 30 and May 15, marked by the appearance of an anticyclonic circulation especially from the three eastern moorings, C2, B3 and A4. The model eddy stayed in the same location for another month. It is difficult to discern from the observations whether or not the eddy was still attached to the Loop Current. By the end of June, the model eddy started to drift westward. The observations agreed well with the model, showing clearly the complete separation of Eddy Franklin.

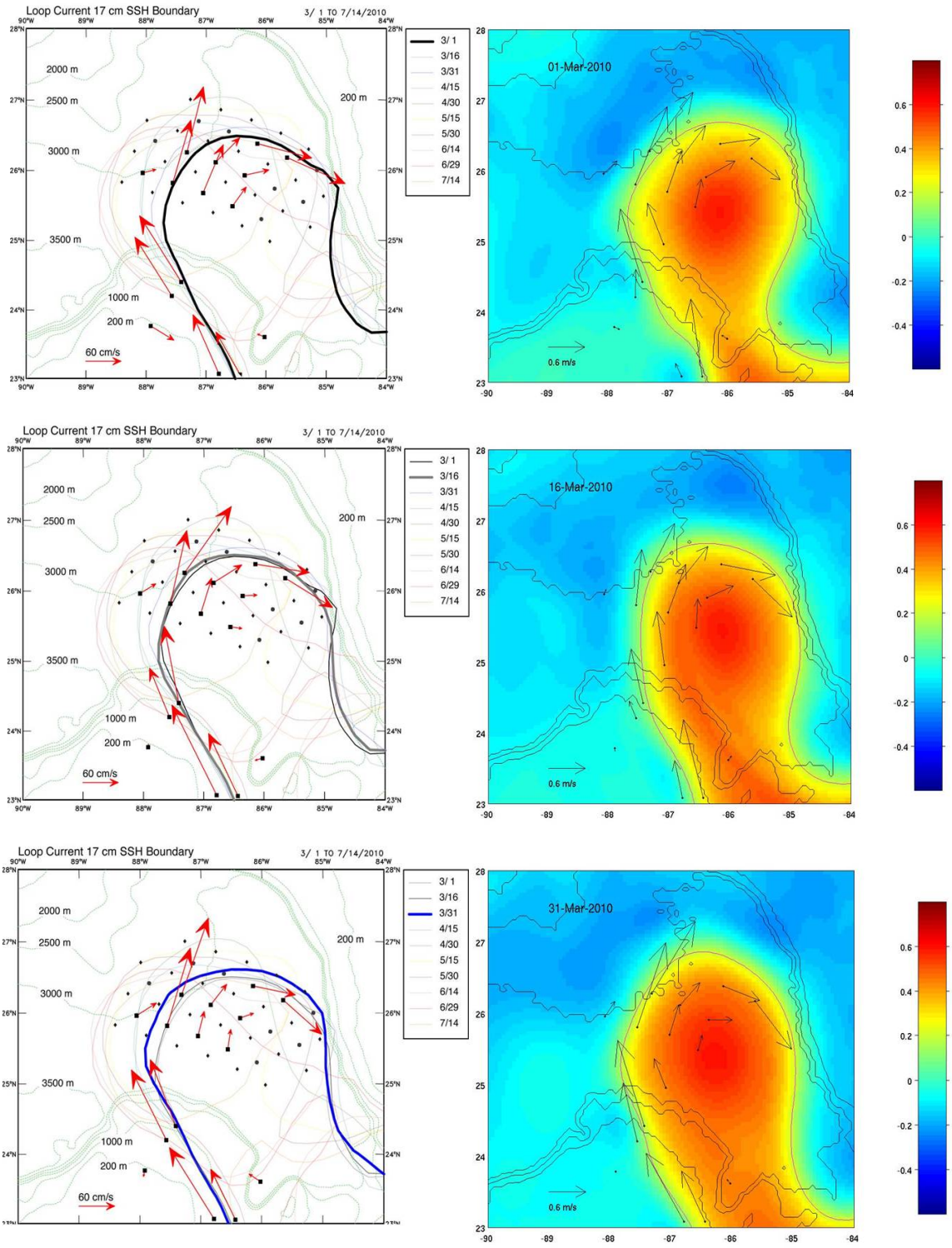

Figure 26. On the right column, IASNFS reanalysis currents at 80 m and SSH (area average removed) with 0.17 m contour marked, and on the left column, the corresponding mooring measurements. The Loop Current and Loop Current Eddy frontal locations on the left column are derived from satellite altimeter SSH analysis.

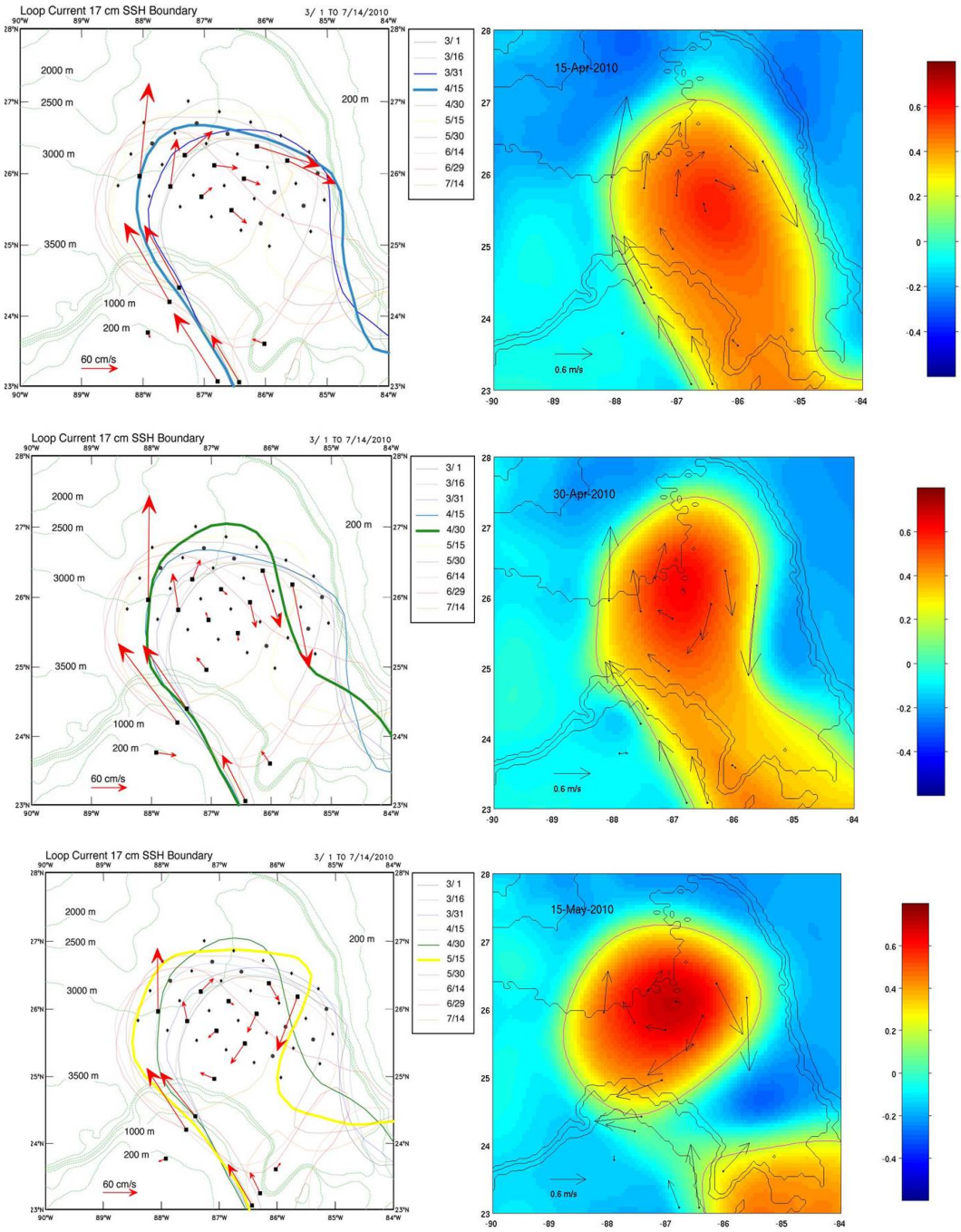

Figure 26. Continued

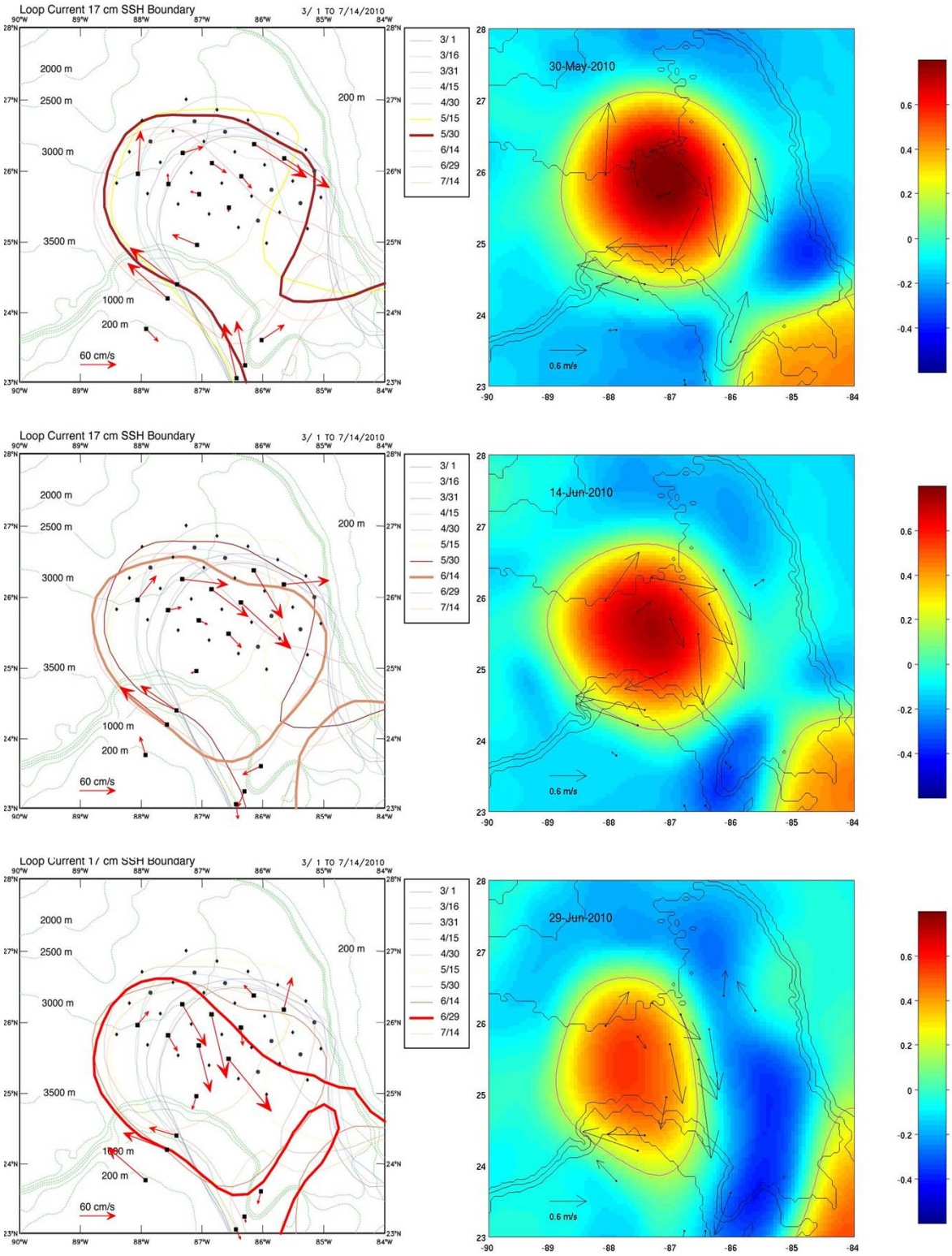

Figure 26. Continued.

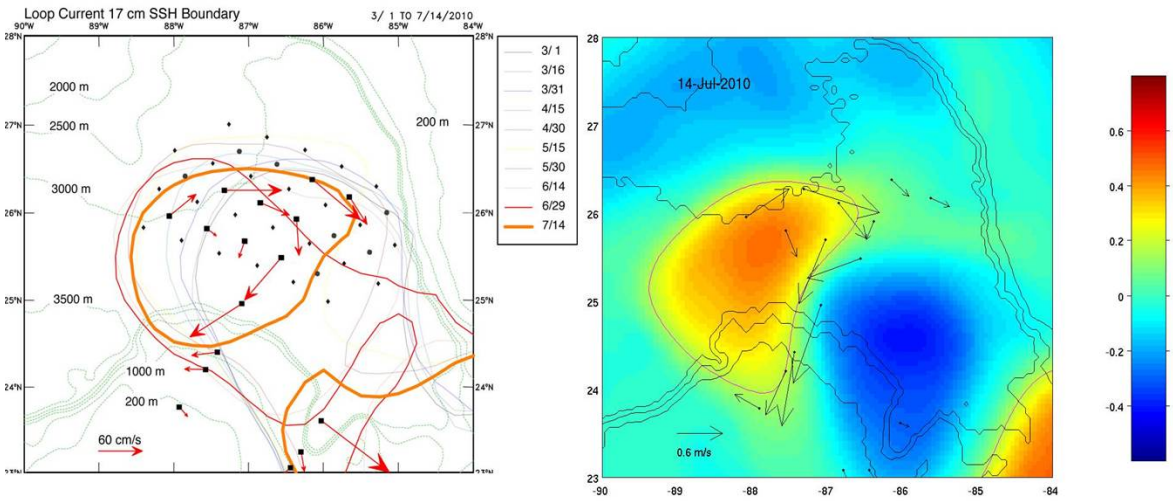

Figure 26. Continued.

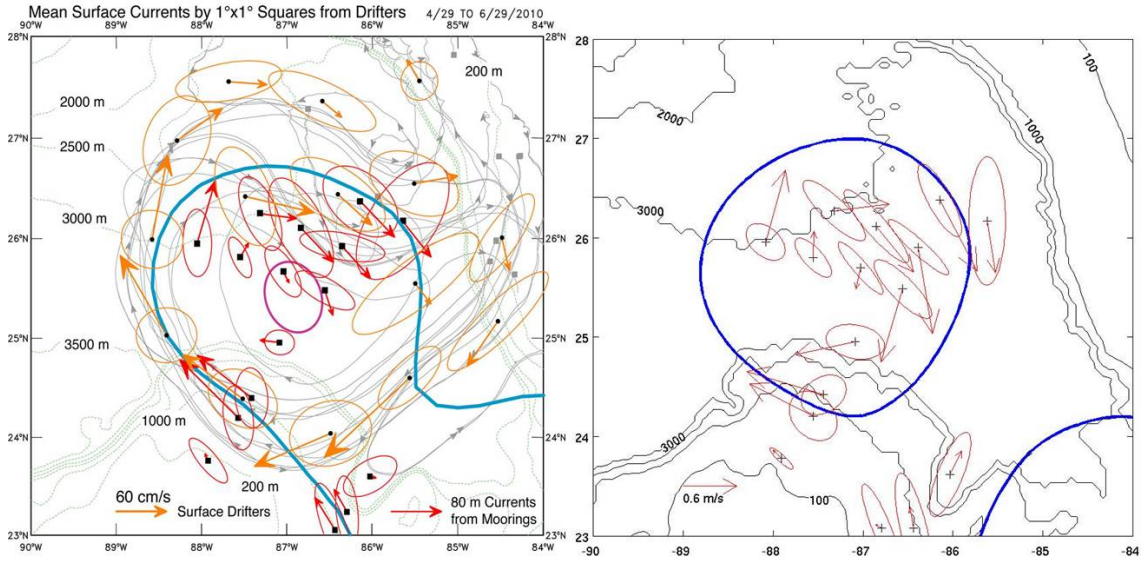

Figure 27. Mean surface velocities and current ellipses from (left) observations and (right) model for May and June 2010. The observations also included estimates from surface drifters, which were not considered in the model.

Figure 27 shows mean velocities and current ellipses from the observations and model for May and June 2010. The general agreement once more is quite remarkable. This suggests that the IASNFS ocean current reanalysis is credible even in resolving mesoscale/frontal processes. It is perhaps then not too surprising that the IASNFS has been successfully employed during the Deep Water Horizon oil spill (Figure 1) as well as in many other transport and mixing studies in the northern Gulf of Mexico.

8 Summary

A multi-model approach was proposed by BOEM to better assess the potential impact of an oil spill on the environment of the Gulf of Mexico by conducting ensemble OSRA model runs. Different sets of model-simulated surface currents and their corresponding surface winds in the Gulf are needed to drive the OSRA model. A 10-year ocean re-analysis for the Gulf of Mexico based on NRL IASNFS has been produced to support this effort.

The reanalysis was derived with NOGAPS atmospheric forcing and assimilation of satellite altimeter sea surface height and MCSST. The open boundary conditions were taken from Navy's Global NCOM. Details of the ocean model, the NOGAPS forcing, the data and data assimilation were described. The output of the reanalysis was examined. It includes evaluations against satellite altimeter measurements, coastal sea levels from tide gauges, sea surface temperatures from buoys and satellites, and ocean currents from moorings. Overall, it shows IASNFS reanalysis is highly correlated with observations and demonstrates a strong model skill indicating that the IASNFS reanalysis is very well produced.

Ten-years-long monthly data sets at 3-hourly interval from 2003 to 2012 within the Gulf of Mexico and Straits of Florida have been prepared and provided to BOME for the ensemble OSRA model run.

References

Akima, H. (1970), A new method of interpolation and smooth curve fitting based on local procedures, *J. Assoc. Comput. Mach*., 17, 589-602.

Allee, R. J., J. C. Kurtz, R. W. Gould, D. S. Ko, K. L. Goodin, and M. Finkbeiner (2014), Application of the coastal and marine ecological classification standard using satellite-derived and modeled data products for pelagic habitats in the northern Gulf of Mexico, *Ocean and Coastal Management*, 88, 13-20, http://dx.doi.org/10.1016/j.ocecoaman.2013.10.021.

Arnone, R. A., B. Casey, D. Ko, P. Flynn, L. Carrolo, and S. Landner (2007), Forecasting coastal optical properties using ocean color and coastal circulation models, *Proc. SPIE*, 6680, doi:10.1117/12.737201.

Arnone, R. A., B. Casey, S. Ladner, D. S. Ko, and R. W. Gould (2010), Forecasting the Coastal Optical Properties using Satellite Ocean Color, in *Oceanography from Space*, eds. V. Barale et al., 335-348, Springer Science+Business Media B. V., doi:10.1007/978-90-481-8681-5_19.

Barron, C. N., A. B. Kara, H. E. Hurlburt, C. Rowley, and L. F. Smedstad (2004), Sea surface height predictions from the global Navy Coastal Ocean Model (NCOM) during 1998–2001, *J. Atmos. Oceanic Technol*., 21, 1876–1894.

Blumberg, A. F., and G. L. Mellor (1987), A description of a three-dimensional coastal ocean circulation model, in *Three-Dimensional Coastal Ocean Models*, ed. N. Heaps, Coastal and Estuarine Sci., 4, 1–16, AGU, Washington, D.C.

Carnes, M. R., D. N. Fox, R. C. Rhodes, and O. M. Smedstad (1996), Data assimilation in a North Pacific Ocean monitoring and prediction system. In *Modern approaches to data assimilation in ocean modeling*, ed. P. Malanotte-Rizzoli, Elsevier Oceanogr. Ser., 61, 319–345, Elsevier, Amsterdam, doi:10.1016/S0422-9894(96)80015-8.

Carnes, M. R. (2000), Description and Evaluation of GDEM-V3.0, NRL Rep. NRL/MR/7330-09-9165, 21 pp., Nav. Res. Lab., Stennis Space Cent., Miss.

Chaichitehrani, N., E. J. D'Sa, D. S. Ko, N. Walker, C. L. Osburn, and R. F. Chen (2014), Colored dissolved organic matter dynamics in the northern Gulf of Mexico from ocean color and numerical model results, *J. Coast. Res*., 30, 800-814, doi: 10.2112/JCOASTRES-D-13-00036.1.

Chapman, D. C., D. S. Ko, and R. H. Preller (2004), A high-resolution numerical modeling study of subtidal circulation in the northern South China Sea, *IEEE J. Ocean. Eng*., 29, 1087-1104, doi: 10.1109/JOE.2004.838334.

Chassignet, E. P., H. E. Hurlburt, O. M. Smedstad, C. N. Barron, D. S. Ko, R. C. Rhodes, J. F. Shriver, A. J. Wallcraft, and R. A. Arnone (2005), Assessment of Data Assimilative Ocean Models in the Gulf of Mexico Using Ocean Color, Geophysical Monography 161 - *Circulation in the Gulf of Mexico: Observations and Models*, eds. W. Sturgers and A. Lugo-Fernandes, 87-100, AGU, Washington, D.C.

D'Sa, E. J., and D. S. Ko (2008), Short-term influences on suspended particulate matter distribution in the northern Gulf of Mexico: Satellite and model observations, *Sensors*, 8, 4249-4264, doi:10.3390/s8074249.

D'Sa, E., M. Korobkin, and D. S. Ko (2011), Effects of Hurricane Ike on the Louisiana-Texas coast from satellite and model data, *Remote Sensing Lett*., 2, 11-19, doi:10.1080/ 01431161.2010.489057.

Ducet, N., P. Y. Le Traon, G. Reverdin (2000), Global high-resolution mapping of ocean circulation from the TOPEX/Poseidon and ERS-1 and -2. *J. Geophys. Res*., 105, 19477–19498.

Egbert, G. D., and S. Y. Erofeeva (2003), Efficient inverse modeling of barotropic ocean tides, *J. Atmos. Oceanic Technol*., 19, 183–204.

Flather, R. A., and R. Proctor (1983), Prediction of North Sea storm surges using numerical models: Recent developments in the U.K., in *North Sea Dynamics*, edited by J. Sundermann and W. Lenz, 299–317, Springer, New York.

Fox, D. N., W. J. Teague, C. N. Barron, M. R. Carnes, and C. M. Lee (2002), The Modular Ocean Data Assimilation System (MODAS), *J. Atmos. Oceanic Technol*., *19*, 240–252, doi:10.1175/1520-0426(2002) 019<0240:TMODAS>2.0.CO;2.

Green, R. E., R. W. Gould, and D. S. Ko (2008), Statistical models for sediment/detritus and dissolved absorption coefficients in coastal waters of the northern Gulf of Mexico, *Cont. Shelf Res*., 28, 1273-1285.

Haltrin, V. I., R. A. Arnone, P. Flynn, B. Casey, A. D. Weidemann, and D. S. Ko (2007), Restoring number of suspended particles in ocean using satellite optical images and forecasting particle fields, *Proc. SPIE*, 6615, doi: 10.1117/12.740435.

Hamilton, P. (2013), unpublished presentation, Science Applications International Corporation.

Haney, R. L. (1991), On the pressure gradient force over steep topography in sigma co-ordinate ocean models, *J. Phys. Oceanogr*., 21, 610-619.

Hetland, R. D. (2010), The effects of mixing and spreading on density in near-field river plumes, *Dyn. Atmos. Oceans*, 49, 37-53, doi:10.1016/j.dynatmoce.2008.11.003.

Holland, W. R., J. C. Chow, and F. O. Bryan (1998), Application of a third-order upwind scheme in the NCAR Ocean Model, *J. Clim*., 11, 1487–1493.

Jacobs, G. A., C. N. Barron, D. N. Fox, K. R. Whitmer, S. Klingenberer, D. May and J. P. Blaha (2002), Operational altimeter sea level products, *Oceanography*, 15, 13-21.

Jerlov, N. G. (1964), Optical classification of ocean water, in *Physical aspects of light in the sea*, ed. Tyler J. E., 45-49, U. Hawaii Press, Honolulu.

Ko, D. S. (2009), IASNFS: An operational real-time nowcast/forecast system for Intra-Americas Sea, in *Proceedings: USA-Mexico workshop on the deepwater physical oceanography of the Gulf of Mexico, June 2007*, eds. C.N.K. Mooers and A. Lugo-Fernández, 95-106, U.S. Dept. of the Interior, Minerals Management Service, Gulf of Mexico OCS Region, New Orleans, LA, OCS Study MMS 2010-001.

Ko, D. S., and Z. Li (2013), A decadal ocean reanalysis for the Gulf of Mexico, Presentation presented at the GoM Oil Spill & Ecosystem Science Conference, New Orleans, LA.

Ko, D. S., R. H. Preller, and P. J. Martin (2003), An experimental real-time Intra-Americas Sea Ocean Nowcast/Forecast System for coastal prediction, paper presented at the AMS 5th Conference on Coastal Atmospheric and Oceanic Prediction and Processes, *Seattle, Wash*., 97–100, AMS, Boston, Mass.

Ko, D. S., P. J. Martin, C. D. Rowley, and R. H. Preller (2008), A real-time coastal ocean prediction experiment for MREA04, *J Mar. Syst*., *69*, 17–28, doi:10.1016/j.jmarsys.2007.02.022.

Lehrter, J., D. S. Ko, M. Murrell, G. Richard, H. James, S. Blake, R. W. Gould, and B. Penta (2013), Nutrient transports and source/sink dynamics on the inner Louisiana continental shelf, *J. Geophys. Res*., 118, 4822-4838, doi:10.1002/jgrc.20362.

Martin, P. J. (2000), *A Description of the Navy Coastal Ocean Model Version 1.0*, NRL Rep. NRL/FR/7322-00-9962, 42 pp., Nav. Res. Lab., Stennis Space Cent., Miss.

Mellor, G. L. (1991), An equation of state for numerical models of oceans and estuaries, *J. Atmos. Oceanic Technol.*, 8, 609–611.

Mellor, G. L., and T. Yamada (1974), A hierarchy of turbulence closure models for planetary boundary layers, *J. Atmos. Sci*., 31, 1791–1806.

Mendoza, W. G., R. G. Zika, J. E. Corredor, D. S. Ko, and C. N. K. Mooers (2009), Developmental strategy for effective sampling to detect possible nutrient fluxes in oligotrophic coastal reef waters in the Caribbean, *J. Operational Oceanogr*., 2, 35-47.

Nash, J. E., and J. V. Sutcliffe (1970), River flow forecasting through conceptual models: Part 1. A discussion of principles, *J. Hydrology*, 10, 282-290.

Pearson, K. (1895), Notes on regression and inheritance in the case of two parents, *Proceedings of the Royal Society of London*, 58, 240–242.

Rhodes, R. C., H. E. Hurlburt, A. J. Wallcraft, C. N. Barron, P. J. Martin, O. M. Smedstad, S. Cross, E. J. Metzger, J. Shriver, A. Kara, and D. S. Ko (2002), Navy real-time global modeling system, Oceanography 15, 29–43. doi: http://dx.doi.org/10.5670/oceanog.2002.34.

Rosmond T. E. (1992), The design and testing of the Navy Operational Global Atmospheric Prediction System, *Weather Forecast*, *7*, 262–272. doi:10.1175/1520-0434(1992).

Shapiro, R. (1970), Smoothing, filtering and boundary effects, *Rev. Geophys. Space Phys*., 8, 359–387.

Shapiro, R. (1975), Linear filtering, *Math. Comp*., 29, 1094–1097.

Teague, W. J., E. J. Molinelli, M. J. Carron (1987), A New System for Management of the "Master Oceanographic Observation Data Set" (MOODS), *EOS*, 68, 553, 558-559.

Appendix

Sample of netCDF file without data body for January 2003:

```
netcdf iasnfs_200301 {
dimensions:
        time = UNLIMITED ; // (248 currently)
        longitude = 359 ;
        latitude = 258 ;
        depth = 40 ;
variables:
        float time(time) ;
                time:long_name = "elapse time" ;
                time:units = "day since 2003-01-01 00:00:00" ;
                time:time_origin = "01-JAN-2003 00:00:00" ;
        float longitude(longitude) ;
                longitude:long_name = "longitude" ;
                longitude:units = "degree east" ;
        float latitude(latitude) ;
                latitude:long_name = "latitude" ;
                latitude:units = "degree north" ;
        float depth(depth) ;
                depth:long_name = "depth" ;
                depth:units = "m" ;
        float uwind(time, latitude, longitude) ;
                uwind:long_name = "u-component 10-m wind speed" ;
                uwind:units = "m/s" ;
                uwind:missing_value = -1.e+34f ;
                uwind:_FillValue = -1.e+34f ;
        float vwind(time, latitude, longitude) ;
                vwind:long_name = "v-component 10-m wind speed" ;
                vwind:units = "m/s" ;
                vwind:missing_value = -1.e+34f ;
                vwind:_FillValue = -1.e+34f ;
        float ssh(time, latitude, longitude) ;
                ssh:long_name = "surface elevation" ;
```

```
        ssh:units = "m" ;
        ssh:missing_value = -1.e+34f ;
        ssh:_FillValue = -1.e+34f ;
    float temperature(time, depth, latitude, longitude) ;
        temperature:long_name = "potential temperature" ;
        temperature:units = "deg C" ;
        temperature:missing_value = -1.e+34f ;
        temperature:_FillValue = -1.e+34f ;
    float salinity(time, depth, latitude, longitude) ;
        salinity:long_name = "salinity" ;
        salinity:units = "ppt" ;
        salinity:missing_value = -1.e+34f ;
        salinity:_FillValue = -1.e+34f ;
    float u(time, depth, latitude, longitude) ;
        u:long_name = "u-velocity" ;
        u:units = "m/s" ;
        u:missing_value = -1.e+34f ;
        u:_FillValue = -1.e+34f ;
    float v(time, depth, latitude, longitude) ;
        v:long_name = "v-velocity" ;
        v:units = "m/s" ;
        v:missing_value = -1.e+34f ;
        v:_FillValue = -1.e+34f ;

// global attributes:
        :source = "IASNFS_Reanalysis" ;
        :title = "v1.0" ;
data:

 time = 0, 0.125, 0.25, 0.375, 0.5, 0.625, 0.75, 0.875, 1, 1.125, 1.25, 1.375, 1.5, 1.625, 1.75,
    1.875, 2, 2.125, 2.25, 2.375, 2.5, 2.625, 2.75, 2.875, 3, 3.125, 3.25, 3.375, 3.5, 3.625,
    3.75, 3.875, 4, 4.125, 4.25, 4.375, 4.5, 4.625, 4.75, 4.875, 5, 5.125, 5.25, 5.375, 5.5,
    5.625, 5.75, 5.875, 6, 6.125, 6.25, 6.375, 6.5, 6.625, 6.75, 6.875, 7, 7.125, 7.25, 7.375,
    7.5, 7.625, 7.75, 7.875, 8, 8.125, 8.25, 8.375, 8.5, 8.625, 8.75, 8.875, 9, 9.125, 9.25,
    9.375, 9.5, 9.625, 9.75, 9.875, 10, 10.125, 10.25, 10.375, 10.5, 10.625, 10.75, 10.875,
    11, 11.125, 11.25, 11.375, 11.5, 11.625, 11.75, 11.875, 12, 12.125, 12.25, 12.375,
```

12.5, 12.625, 12.75, 12.875, 13, 13.125, 13.25, 13.375, 13.5, 13.625, 13.75, 13.875, 14, 14.125, 14.25, 14.375, 14.5, 14.625, 14.75, 14.875, 15, 15.125, 15.25, 15.375, 15.5, 15.625, 15.75, 15.875, 16, 16.125, 16.25, 16.375, 16.5, 16.625, 16.75, 16.875, 17, 17.125, 17.25, 17.375, 17.5, 17.625, 17.75, 17.875, 18, 18.125, 18.25, 18.375, 18.5, 18.625, 18.75, 18.875, 19, 19.125, 19.25, 19.375, 19.5, 19.625, 19.75, 19.875, 20, 20.125, 20.25, 20.375, 20.5, 20.625, 20.75, 20.875, 21, 21.125, 21.25, 21.375, 21.5, 21.625, 21.75, 21.875, 22, 22.125, 22.25, 22.375, 22.5, 22.625, 22.75, 22.875, 23, 23.125, 23.25, 23.375, 23.5, 23.625, 23.75, 23.875, 24, 24.125, 24.25, 24.375, 24.5, 24.625, 24.75, 24.875, 25, 25.125, 25.25, 25.375, 25.5, 25.625, 25.75, 25.875, 26, 26.125, 26.25, 26.375, 26.5, 26.625, 26.75, 26.875, 27, 27.125, 27.25, 27.375, 27.5, 27.625, 27.75, 27.875, 28, 28.125, 28.25, 28.375, 28.5, 28.625, 28.75, 28.875, 29, 29.125, 29.25, 29.375, 29.5, 29.625, 29.75, 29.875, 30, 30.125, 30.25, 30.375, 30.5, 30.625, 30.75, 30.875;

longitude = 262.016, 262.075, 262.133, 262.192, 262.25, 262.309, 262.367, 262.426, 262.485, 262.543, 262.602, 262.661, 262.719, 262.778, 262.836, 262.895, 262.953, 263.012, 263.07, 263.129, 263.188, 263.246, 263.305, 263.364, 263.422, 263.481, 263.54, 263.598, 263.657, 263.715, 263.774, 263.832, 263.891, 263.949, 264.008, 264.067, 264.125, 264.184, 264.243, 264.301, 264.36, 264.419, 264.477, 264.536, 264.594, 264.653, 264.711, 264.77, 264.828, 264.887, 264.946, 265.004, 265.063, 265.122, 265.18, 265.239, 265.297, 265.356, 265.414, 265.473, 265.531, 265.59, 265.649, 265.707, 265.766, 265.825, 265.883, 265.942, 266.001, 266.059, 266.118, 266.176, 266.235, 266.293, 266.352, 266.41, 266.469, 266.528, 266.586, 266.645, 266.704, 266.762, 266.821, 266.879, 266.938, 266.996, 267.055, 267.113, 267.172, 267.231, 267.289, 267.348, 267.407, 267.465, 267.524, 267.583, 267.641, 267.7, 267.758, 267.817, 267.875, 267.934, 267.992, 268.051, 268.11, 268.168, 268.227, 268.286, 268.344, 268.403, 268.462, 268.52, 268.579, 268.637, 268.696, 268.754, 268.813, 268.871, 268.93, 268.989, 269.047, 269.106, 269.165, 269.223, 269.282, 269.34, 269.399, 269.457, 269.516, 269.574, 269.633, 269.692, 269.75, 269.809, 269.868, 269.926, 269.985, 270.044, 270.102, 270.161, 270.219, 270.278, 270.336, 270.395, 270.453, 270.512, 270.571, 270.629, 270.688, 270.747, 270.805, 270.864, 270.922, 270.981, 271.039, 271.098, 271.156, 271.215, 271.274, 271.332, 271.391, 271.45, 271.508, 271.567, 271.626, 271.684, 271.743, 271.801, 271.86, 271.918, 271.977, 272.035, 272.094, 272.153, 272.211, 272.27, 272.329, 272.387, 272.446, 272.504, 272.563, 272.621, 272.68, 272.738, 272.797, 272.856, 272.914, 272.973, 273.032, 273.09, 273.149, 273.208, 273.266, 273.325, 273.383, 273.442, 273.5,

273.559, 273.617, 273.676, 273.735, 273.793, 273.852, 273.911, 273.969, 274.028, 274.086, 274.145, 274.203, 274.262, 274.32, 274.379, 274.438, 274.496, 274.555, 274.614, 274.672, 274.731, 274.79, 274.848, 274.907, 274.965, 275.024, 275.082, 275.141, 275.199, 275.258, 275.317, 275.375, 275.434, 275.493, 275.551, 275.61, 275.669, 275.727, 275.786, 275.844, 275.903, 275.961, 276.02, 276.078, 276.137, 276.196, 276.254, 276.313, 276.372, 276.43, 276.489, 276.547, 276.606, 276.664, 276.723, 276.781, 276.84, 276.899, 276.957, 277.016, 277.075, 277.133, 277.192, 277.251, 277.309, 277.368, 277.426, 277.485, 277.543, 277.602, 277.66, 277.719, 277.778, 277.836, 277.895, 277.954, 278.012, 278.071, 278.129, 278.188, 278.246, 278.305, 278.363, 278.422, 278.481, 278.539, 278.598, 278.657, 278.715, 278.774, 278.833, 278.891, 278.95, 279.008, 279.067, 279.125, 279.184, 279.242, 279.301, 279.36, 279.418, 279.477, 279.536, 279.594, 279.653, 279.712, 279.77, 279.829, 279.887, 279.946, 280.004, 280.063, 280.121, 280.18, 280.239, 280.297, 280.356, 280.415, 280.473, 280.532, 280.59, 280.649, 280.707, 280.766, 280.824, 280.883, 280.942, 281, 281.059, 281.118, 281.176, 281.235, 281.294, 281.352, 281.411, 281.469, 281.528, 281.586, 281.645, 281.703, 281.762, 281.821, 281.879, 281.938, 281.997, 282.055, 282.114, 282.172, 282.231, 282.289, 282.348, 282.406, 282.465, 282.524, 282.582, 282.641, 282.7, 282.758, 282.817, 282.876, 282.934, 282.993;

latitude = 16.973, 17.029, 17.085, 17.141, 17.197, 17.253, 17.309, 17.365, 17.42, 17.476, 17.532, 17.588, 17.644, 17.7, 17.755, 17.811, 17.867, 17.923, 17.979, 18.035, 18.09, 18.146, 18.202, 18.257, 18.313, 18.369, 18.424, 18.48, 18.535, 18.591, 18.646, 18.702, 18.757, 18.813, 18.868, 18.924, 18.979, 19.034, 19.09, 19.145, 19.2, 19.256, 19.311, 19.366, 19.422, 19.477, 19.532, 19.588, 19.643, 19.698, 19.753, 19.808, 19.863, 19.918, 19.973, 20.028, 20.083, 20.138, 20.193, 20.248, 20.303, 20.358, 20.413, 20.468, 20.523, 20.578, 20.633, 20.688, 20.742, 20.797, 20.852, 20.906, 20.961, 21.016, 21.07, 21.125, 21.18, 21.234, 21.289, 21.344, 21.398, 21.453, 21.508, 21.562, 21.617, 21.671, 21.726, 21.78, 21.834, 21.889, 21.943, 21.997, 22.052, 22.106, 22.16, 22.215, 22.269, 22.323, 22.377, 22.431, 22.485, 22.54, 22.594, 22.648, 22.702, 22.756, 22.81, 22.864, 22.918, 22.972, 23.026, 23.08, 23.134, 23.187, 23.241, 23.295, 23.349, 23.403, 23.457, 23.51, 23.564, 23.618, 23.671, 23.725, 23.779, 23.832, 23.886, 23.939, 23.993, 24.046, 24.1, 24.153, 24.207, 24.26, 24.314, 24.367, 24.42, 24.474, 24.527, 24.58, 24.634, 24.687, 24.74, 24.794, 24.847, 24.9, 24.953, 25.006, 25.059, 25.112, 25.165, 25.218, 25.271, 25.324, 25.377, 25.43, 25.483, 25.536, 25.589, 25.642, 25.695, 25.747, 25.8, 25.853, 25.905, 25.958, 26.011, 26.063, 26.116, 26.169, 26.221, 26.274, 26.326, 26.379, 26.431, 26.484, 26.536, 26.589, 26.641, 26.694, 26.746, 26.798, 26.85,

26.902, 26.954, 27.007, 27.059, 27.111, 27.164, 27.216, 27.268, 27.32, 27.372, 27.424, 27.476, 27.528, 27.58, 27.632, 27.684, 27.736, 27.787, 27.839, 27.891, 27.942, 27.994, 28.046, 28.097, 28.149, 28.201, 28.252, 28.304, 28.356, 28.407, 28.459, 28.51, 28.562, 28.613, 28.665, 28.716, 28.768, 28.819, 28.871, 28.922, 28.973, 29.024, 29.075, 29.126, 29.178, 29.229, 29.28, 29.331, 29.382, 29.433, 29.484, 29.535, 29.586, 29.637, 29.688, 29.739, 29.79, 29.841, 29.892, 29.942, 29.993, 30.044, 30.094, 30.145, 30.196, 30.246, 30.297, 30.348, 30.398, 30.449, 30.499, 30.55, 30.6, 30.65, 30.701;

depth = 0.5, 1.5949, 2.89763, 4.44763, 6.29183, 8.48608, 11.0968, 14.2031, 17.899, 22.2964, 27.5284, 33.7536, 41.1603, 49.9729, 60.4583, 72.9338, 87.7773, 105.438, 126.451, 151.453, 181.2, 216.594, 258.705, 308.81, 368.425, 439.356, 523.749, 624.162, 743.634, 885.782, 1054.91, 1256.14, 1495.57, 1780.45, 2119.39, 2522.67, 3002.5, 3573.4, 4252.67, 5060.87;

The Department of the Interior Mission

As the Nation's principal conservation agency, the Department of the Interior has responsibility for most of our nationally owned public lands and natural resources. This includes fostering sound use of our land and water resources; protecting our fish, wildlife, and biological diversity; preserving the environmental and cultural values of our national parks and historical places; and providing for the enjoyment of life through outdoor recreation. The Department assesses our energy and mineral resources and works to ensure that their development is in the best interests of all our people by encouraging stewardship and citizen participation in their care. The Department also has a major responsibility for American Indian reservation communities and for people who live in island territories under US administration.

BOEM
Bureau of Ocean Energy Management

The Bureau of Ocean Energy Management

As a bureau of the Department of the Interior, the Bureau of Ocean Energy (BOEM) primary responsibilities are to manage the mineral resources located on the Nation's Outer Continental Shelf (OCS) in an environmentally sound and safe manner.

The BOEM Environmental Studies Program

The mission of the Environmental Studies Program (ESP) is to provide the information needed to predict, assess, and manage impacts from offshore energy and marine mineral exploration, development, and production activities on human, marine, and coastal environments.